Bulletin of the Seismological Society of America, Vol. 94, No. 6, pp. 2380–2399, December 2004

Ⓔ

Plate-Tectonic Analysis of Shallow Seismicity: Apparent Boundary Width, Beta, Corner Magnitude, Coupled Lithosphere Thickness, and Coupling in Seven Tectonic Settings

by Peter Bird and Yan Y. Kagan

Abstract A new plate model is used to analyze the mean seismicities of seven types of plate boundary (CRB, continental rift boundary; CTF, continental transform fault; CCB, continental convergent boundary; OSR, oceanic spreading ridge; OTF, oceanic transform fault; OCB, oceanic convergent boundary; SUB, subduction zone). We compare the platelike (nonorogen) regions of model PB2002 (Bird, 2003) with the centroid moment tensor (CMT) catalog to select apparent boundary half-widths and then assign 95% of shallow earthquakes to one of these settings. A tapered Gutenberg-Richter model of the frequency/moment relation is fit to the subcatalog for each setting by maximum likelihood. Best-fitting β values range from 0.53 to 0.92, but all 95% confidence ranges are consistent with a common value of 0.61–0.66. To better determine some corner magnitudes we expand the subcatalogs by (1) inclusion of orogens and (2) inclusion of years 1900–1975 from the catalog of Pacheco and Sykes (1992). Combining both earthquake statistics and the plate-tectonic constraint on moment rate, corner magnitudes include the following: CRB, $7.64^{+0.76}_{-0.26}$; CTF, $8.01^{+0.47}_{-0.21}$; CCB, $8.46^{+0.21}_{-0.39}$; OCB, $8.04^{+0.52}_{-0.22}$; and SUB, $9.58^{+0.48}_{-0.46}$. Coupled lithosphere thicknesses are found to be the following: CRB, $3.0^{+7.0}_{-1.4}$; CTF, 8.6^{+11}_{-4}; CCB, $18^{+?}_{-11}$; OSR, $0.13^{+0.13}_{-0.09}$ for normal faulting and $0.40^{+?}_{-0.21}$ for strike slip; OTF, $13^{+?}_{-7.3}$, $1.8^{+1.1}_{-0.5}$, and $1.6^{+1.1}_{-0.5}$ at low, medium, and high velocities; OCB, $3.8^{+13.7}_{-2.3}$; and SUB, $18.0^{+?}_{-10.8}$. In general, high coupling of subduction and continental plate boundaries suggests that here all seismic gaps are dangerous unless proven to be creeping. In general, low coupling within oceanic lithosphere suggests a different model of isolated seismic fault patches surrounded by large seismic gaps that may be permanent.

Online Material: Global seismic subcatalogs of shallow earthquakes.

Introduction

Since the introduction of plate-tectonic theory four decades ago, it has been widely expected to provide a basis for quantitative prediction of long-term-average seismicity and seismic hazard. This promise has not been fully realized because of several problems: (1) Early models with 12–14 plates gave seriously oversimplified kinematic predictions in some of the most seismically active areas (e.g., the southwest Pacific). (2) Some regions are so complex that it is doubtful whether any rigid-plate model can adequately describe them (e.g., Tibet Plateau and North Fiji Basin). (3) It is not resolved whether seismic coupling is nearly perfect, or highly variable, within the cold frictional seismogenic layer of the lithosphere. This question is difficult to answer in any regional study because the instrumental seismic record only covers one century, whereas there are good indications of seismic cycles lasting five centuries in some plate boundaries (e.g., Cascadia and South Chile trenches) and many centuries in plate interiors.

The plate model of Bird (2003) was specifically constructed to address the first two problems. Instead of 14 plates, it has 52, allowing most of the complexity of the Pacific margin to be described. It explicitly excludes the most complex regions as "orogens." This new global model allows the third problem to be addressed by use of the ergodic assumption: for studies of globally uncorrelated behavior, data collected widely in space can substitute for local data collected over long times. By merging the behavior of all subduction zones or all continental transform faults worldwide for a century, we may have enough information to extract their average seismicity properties with confidence limits that are small enough to be useful.

The model of Bird (2003) also explicitly classifies each

short plate-boundary step (interval) as belonging to one of seven classes: continental rift boundary (CRB), continental transform fault (CTF), continental convergent boundary (CCB), oceanic spreading ridge (OSR), oceanic transform fault (OTF), oceanic convergent boundary (OCB), and subduction zone (SUB). We first consider the reasons why earthquake epicenters do not lie precisely on plate boundaries and adopt a rule for selecting the apparent seismic half-widths of plate-boundaries. Then, we use a probabilistic approach to match shallow earthquakes with particular plate-boundary segments by searching for the best match between earthquake properties. Then, we collect the earthquakes into eight subcatalogs, corresponding to seven plate-boundary types and plate interiors. We analyze each subcatalog by maximum-likelihood methods to determine the parameters of its tapered Gutenberg-Richter frequency/moment relation (Kagan, 2002a). Finally, we integrate these distributions to estimate the long-term-average moment rate for each class and compare them with plate tectonic model predictions of the line integrals of relative velocity. From the ratios, we determine coupled lithosphere thicknesses for each type of plate boundary.

Data Sets

The plate-tectonic model used in this study is named PB2002. Bird (2003) described its construction and format, which included explicit mapping of boundary locations. In addition to the 14 large plates of the NUVEL-1 model (DeMets *et al.*, 1990), it includes 38 small plates documented with recent geodetic, bathymetric, and/or seismic data. Euler poles are tabulated for estimation of present relative velocities. Model PB2002 does not claim to achieve a complete description of kinematics on the Earth. Instead, it formally designates 13 "orogen" regions in which the plate model is known to be inaccurate, either due to very many small plates or to nonplatelike behavior. In most phases of this study, seismicity of these orogens will be excluded. However, it will be considered in some cases where we seek to maximize the sizes of subcatalogs of large earthquakes.

Earthquake sizes are best characterized by scalar moment M, but moment magnitude m is also a popular scale. In this project, we used the conversion

$$m = (2/3)(\log_{10}(M) - 9.05) \quad (1)$$

of Hanks and Kanamori (1979). There is confusion because some later authors have used slightly different values of the constant (Kagan, 2003). Magnitudes quoted in this article (as a convenience for readers) should be converted to scalar moments using (1) only.

Our primary seismic catalog is the shallow-earthquake subset of the Harvard Centroid Moment Tensor (CMT) catalog, which was presented in a number of incremental publications (e.g., Dziewonski *et al.*, 1981; Ekström *et al.*, 2003) and which is presently available in digital form at www.seismology.harvard.edu/projects/CMT/. This catalog begins 1 January 1977, and through the cutoff date for this study (30 September 2002) it contains 15,015 events with centroid depth $\leq$70 km. Nuclear tests and other explosions are excluded from CMT. The threshold moment for completeness is $M_t = 3.5 \times 10^{17}$ N m ($m_t \cong 5.66$) overall; for specific years and/or regions, the threshold is sometimes lower (Kagan, 2003). Each solution includes a moment tensor; we make use of the orientations of the principal axes and the scalar moment but do not consider possible non-double-couple source components. Ekström and Nettles (1997) extended the CMT catalog by finding moment tensors of 108 large events (including 98 shallow events) in 1976. If their threshold magnitude is estimated as $M_t \cong 3 \times 10^{18}$ N m ($m_t \cong 6.28$) for shallow events, then there are 59 shallow earthquakes in the complete part.

There are at least three valuable catalogs of the earlier years of the twentieth century (1900–1975): Pacheco and Sykes (1992), Triep and Sykes (1997), and Engdahl and Villaseñor (2002). The first catalog is most convenient for our study because Pacheco and Sykes collected moment determinations from the literature, when available, and scaled 20-sec surface-wave magnitudes to estimated moments for other events. Saturation of surface-wave magnitudes should not greatly affect this catalog, since most of the larger events (all but two of the $m > 8.0$ events) have independently determined moments. Where multiple-moment estimates were available, we accept their selection. In addition, the Pacheco and Sykes (1992) catalog provides limited mechanism information (generic type) for 41% of the events, which is useful in assigning events to the correct tectonic setting. It lists 598 shallow events during 1900–1975 and is complete for shallow earthquakes with surface-wave magnitude $M_s \geq 7$. One peculiarity of the Pacheco and Sykes (1992) catalog is that it lists the two largest earthquakes of the twentieth century as occurring only 1 min apart at virtually the same location: 19:10 versus 19:11 on 22 May 1960, at 38.05/38.20° S, 73.34/73.50° W, 32 km depth, with $m = 9.49$ and 9.64, respectively. The first event apparently refers to the low-frequency precursor detected by both Kanamori and Cipar (1974) and Cifuentes and Silver (1989) 15–19 min before the main shock. Such fault-creep events (also called "slow" or "silent" earthquakes) are rarely detected unless they generate tsunamis or precede famous main shocks. Since it is not possible to include all fault-creep events down to the same moment threshold used for earthquakes, we prefer to drop this one slow precursor event from the catalog. We note that Engdahl and Villaseñor (2002) treated this event in the same way.

Apparent Boundary Half-Widths

To analyze earthquakes by plate setting, it is necessary to associate most shallow earthquakes with nearby plate boundaries, while classifying the remainder as intraplate events. "Apparent boundary half-width" is the term we use

for the maximum horizontal distance between a plate-boundary segment and the epicenter of an associated earthquake. It is a superposition of four characteristic dimensions: (1) half-width of the set of fault traces that make up the boundary zone on the surface; (2) half-width added by nonvertical dip of faults as they extend down through the seismogenic portion of the lithosphere; (3) half-width added by error in the mapped position of the plate boundary; (4) half-width added by earthquake mislocation. We expect that (at least) the first two factors will vary according to boundary type.

Table 1 lists our *a priori* estimates of reasonable half-width ranges for each plate-boundary type. Because these *a priori* apparent half-widths are rather subjective, we also studied histogram and cumulative distributions of the relative frequency of shallow earthquakes with distance. We considered all shallow (≤70 km) earthquakes in the CMT catalog (1 January 1977–30 September 2002) without using any completeness threshold. (Completeness is expected to vary regionally over the Earth, but to be nearly uniform within the narrow width of each of our local distributions.) However, we excluded both earthquakes and plate-boundary segments lying within any of the 13 orogens of model PB2002, because within these regions there is no assurance of platelike behavior.

To reduce the noise contributed to each distribution by adjacent plate boundaries, we count only earthquakes with mechanisms appropriate to the boundary class in question. An earthquake is considered strike slip if its *N* axis is more vertical that either the *P* axis or *T* axis. If the *P* axis is closest to vertical, the event is considered normal, and if the *T* axis is closest to vertical, the event is considered a thrust. Normal-faulting events are associated with the nearest CRB, OSR, or SUB step; strike-slip events are associated with the nearest CTF, OTF, or SUB step; thrusting events are associated with the nearest CCB, OCB, or SUB step. (Subduction zones generate large numbers of normal-faulting earthquakes through the plate-bending process and may also generate strike-slip earthquakes if subduction is oblique.)

For six of the seven boundary classes (except SUB) we count only earthquakes that are "beside" a plate-boundary step of the class under consideration; that is, those that lie within a rectangle that is bisected longitudinally by the step and shares its length. But subduction zone trench boundaries are often oblique to the direction of relative plate motion and, in detail, their trends are highly variable. It is not reasonable to project a perpendicular belt for 276 km (the maximum *a priori* landward half-width) from subduction boundary steps to collect associated earthquakes, and belts from adjacent boundary steps would often overlap or leave gaps. Instead, we measure distance from SUB boundaries along the azimuth of relative plate motion (according to the Euler poles of PB2002). Because of this rule, each SUB boundary step has an associated "lane" of parallelogram shape on the surface, within which epicenters of shallow earthquakes might be considered associated with that step. These lanes are parallel and nonoverlapping, except near triple junctions involving two or three subduction zones.

Histogram and cumulative distributions were computed out to a maximum distance of 300 km, which is based on a compromise between two conflicting considerations. First, the width range examined should be at least the largest apparent half-width expected *a priori* (276 km). Second, the modal plate size in PB2002 is about 1×10^{11} m^2, or (316 km)^2, and the median plate size is 5.2×10^{11} m^2, or (720 km)^2. If we construct distributions much wider than one-half of these typical dimensions, we have to expect increasing interference from other recognized plate boundaries in the outer parts of the distributions. (Interference from unrecognized small-plate boundaries may also be a general problem, but we have no tools for assessing this.)

Cumulative distributions are presented in Figure 1. The distribution for subduction zones is two-sided (distinct land-

Table 1
Estimates of Apparent Boundary Half-Width (in km) and CMT Catalog Statistics

							SUB	
	CRB	CTF	CCB	OSR	OTF	OCB	Landward	Seaward
A priori								
Half-width of fault set	15–35	8–220	0–30	0–15	0–30	?	0–240	~100
Half-width of fault dip	2–20	0–9	17–165	0–5	0–23	17–165	50–150	2–20
Boundary mislocation	25	25–35	25	15–25	15–25	25	19	19
Earthquake mislocation	18–30	18–30	18–30	25–40	25–40	18–30	18–30	18–30
(Combined) expectation	53–94	39–275	48–234	29–67	29–100	61–200?	76–276	~128–155
Empirical								
75% of total count	72	158	106	50	49	91	120	60
90% of total count	127	247	158	93	97	151	179	92
Twice median distance	55	116	116	53	53	84	154	60
Twice mean distance	103	185	146	83	83	130	179	90
Twice rms distance	154	257	189	132	128	186	220	135
Selection								
Selected half-width	154	257	189	132	128	186	220	135

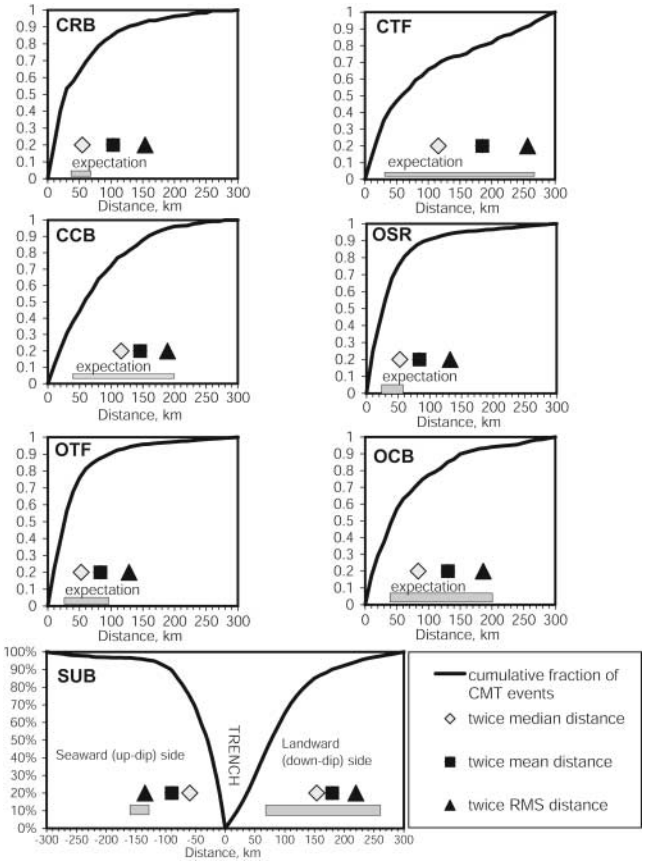

Figure 1. Cumulative counts of shallow earthquakes of appropriate mechanism from the Harvard CMT catalog 1 January 1977 to 30 September 2002, as a function of horizontal distance from the nearest PB2002 plate-boundary segment of a certain class. Plate-boundary segments and earthquakes within orogens of PB2002 have been excluded. "Expectation" bars mark the *a priori* expected ranges of half-widths, based on Table 1. Triangles at twice rms distance indicate the defining half-widths selected for this study. Events outside the defined half-widths are not necessarily intraplate events; in many cases, they will be assigned to other plate boundaries.

ward and seaward sides) based on the obvious asymmetry of these plate boundaries, which was built into model PB2002. For all the other boundary types, a one-sided or symmetrical distribution is presented because there is no obvious objective way to break their (potential) symmetry.

Five metrics of each distribution are listed in Table 1: distance encompassing 75% of events, distance encompassing 90% of events, twice median distance, twice mean distance, and twice root-mean-square (rms) distance. We wish to choose a simple rule, based on one or more of these metrics, to allow consistent and repeatable determination of apparent boundary half-widths as plate models and seismic catalogs change in the future. Apparent half-widths should be large enough to encompass most of the half-width that was expected *a priori*. In general, it is better to adopt larger half-widths, because (1) more earthquakes in the subcatalogs for each class will give better statistical control on their frequency/moment distributions; (2) because some plate-boundary locations have been guided by the locations of the largest earthquakes, it would bias the slope of the log-frequency/log-moment relation to smaller values if we selected too narrow a region around these events; and (3) unless most of the seismicity that is arguably related to plate boundaries is included in moment-rate calculations, the coupled lithosphere thicknesses and coupling coefficients could be biased downward. For all these reasons, we use twice the rms distance as the selected apparent half-width of each boundary class. This is consistent with the tradition of "keeping all data within 2 sigma of the mean," and in fact captures 91.6% to 95.7% of the total earthquake counts in each of these distributions.

Classification of Shallow Earthquakes

Algorithms

Consider a particular shallow earthquake, with hypocenter or centroid at latitude θ, longitude ϕ, and depth z (measured from sea level). Let its moment tensor, normalized to unit scalar moment, be designated $\hat{\hat{M}}$. To associate this earthquake with a particular plate-boundary step of index i, we first estimate $P_i'(\theta,\phi,z,\hat{\hat{M}})$, the relative probability that step i produced this earthquake, for all steps. If $\sup_i\{P_i'\} = 0$, then the earthquake is considered an intraplate event.

For most purposes, the assignment of the earthquake to a step is just a means to assigning the earthquake to a subcatalog for one of the seven plate-boundary classes. It is understood that each of the steps i has previously been designated as belonging to one of the $k = 1, \ldots, 7$ classes defined in model PB2002, so that $k = k(i)$. After relative probabilities are computed for each plate-boundary step, we also sum these by step class to determine the relative probabilities that this particular earthquake was created by each of the seven plate-boundary classes.

We used two variants of this earthquake classification method: (1) Each earthquake is assigned to the plate-boundary step with the highest individual P_i' and takes its class from that step. This results in a set of seven subcatalogs that we call "maximum-probability subcatalogs." (2) A random-number generator is used to assign the earthquake to one of the boundary classes that was represented by a positive sum of P_i' values for steps in that class. The selection bins (with which the random number is compared) have widths in proportion to these sums of P_i'. We call the results "Monte Carlo subcatalogs," and compute five realizations using different seeds for the random-number generator.

A hypothetical example may clarify the difference. An earthquake with an ambiguous focal mechanism occurs near a short OSR segment surrounded by longer OTF segments.

The P_i' for the OSR segment is the largest, but the sum of the P_i' for all OTF segments is greater by a factor of 2. In this case, maximum-likelihood classification assigns the earthquake to OSR, whereas Monte Carlo classification assigns it to OTF two-thirds of the time and to OSR one-third of the time. Each earthquake in each subcatalog file of the electronic supplement (Ⓔ available online at the SSA Web site) displays these relative probabilities summed by class, and the associated documention file explains their format.

In either variant, we approximate the relative probability that step i produced this earthquake by a product of five factors:

$$P_i'(\theta,\phi,z,\hat{\hat{M}}) = A_i B_i(\theta,\phi) \sum_{j=1,5} \left\{ C_{ij} D_{ij}(z,\theta,\phi) E_{ij}(\hat{\hat{M}}) \right\}. \quad (2)$$

A_i is the relative number (or rate) of detectable earthquakes expected on step i, and it is assumed to be composed of a class factor, a length factor, and a velocity factor:

$$A_i = N_k \frac{l_i \, v_i}{L_k \, V_k} \quad (3)$$

where N_k is the number of earthquakes (above threshold moment M_t) produced in nonorogen regions by all steps of class k, ℓ_i is the trace length of step i, L_k is the total trace length (excluding orogens) of all steps in class k, v_i is the relative plate velocity across step i, and V_k is the length-weighted mean relative plate velocity across all steps of class k. The counts N_k are poorly known at the beginning of the classification process but are corrected by iteration of the process to convergence. Final values of $N_k/(L_k V_k)$ may be seen in Table 2.

$B_i(\theta,\phi)$ is the probability density (per unit area) that an earthquake that occurs on step i will appear to occur at the latitude and longitude of the actual earthquake in question (Fig. 2). Using a local coordinate system aligned with step i, we define B as the product of a function of distance f across the step, and another function of distance s along the length of the step: $B_i(\theta,\phi) = X_i(f_i(\theta,\phi)) Y_i(s_i(\theta,\phi))$.

The variation of probability across the step is known from the previous section, which determined apparent half-widths h_k for each of the classes (and two asymmetric half-widths for subduction zones), defined as twice the rms distance of relevant earthquakes from boundaries of that class. Therefore, these half-widths are comparable with twice the standard deviations of normal distributions. Let f_i be the "offset" of surface point (θ,ϕ) from the peak of the seismicity distribution for step i. (This peak occurs on the trace of step i for all classes except subduction zones.) Then, we approximate:

$$X_i \cong \begin{cases} \dfrac{1}{0.95} \dfrac{\sqrt{2}}{\sqrt{\pi} h_k} \exp(-2 f_i^2 / h_k^2); & |f_i| \le h_k \\ 0; & |f_i| > h_k \end{cases} \quad (4)$$

Table 2

Earthquakes per Century, per 100 km of Boundary, Scaled to Plate Velocity 48 mm/a, Based on CMT Catalog (1977–2002)

Symbol	Plate-Boundary Class	$M > 3.5 \times 10^{17}$ N m ($m > 5.66$)	$M > 3.5 \times 10^{19}$ N m ($m > 6.99$)
CRB	Continental Rift Boundary	7.3	0.21
CTF	Continental Transform Fault	8.9	0.39
CCB	Continental Convergent Boundary	22.4	0.79
OSR*	Oceanic Spreading Ridge*	0.9*	0.01*
OTF	Oceanic Transform Fault	8.8	0.06
OCB	Oceanic Convergent Boundary	7.7	0.71
SUB	Subduction Zone	15.9	0.83

*Unlike other boundaries, OSRs have higher seismicity at lower relative plate velocity.

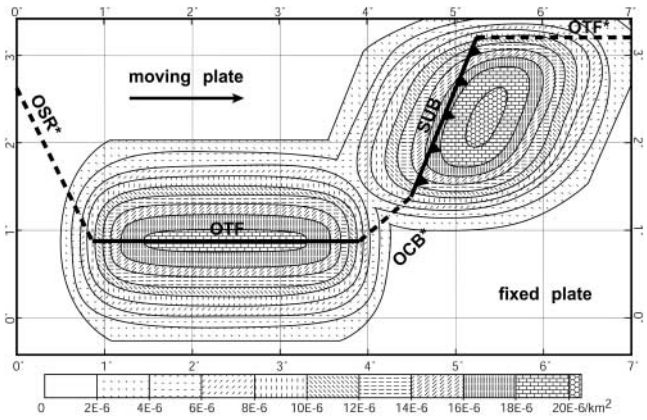

Figure 2. Contour maps of the spatial probability density functions (PDFs) B (equations 2, 4, 5) associated with two generic plate-boundary steps (OTF and SUB). The B functions of the other steps that make up the boundary (OSR,* OCB,* and OTF*) are omitted for clarity in this figure, but they would be considered in actual earthquake classification. Each B function is the product of a Gaussian PDF on an axis crossing the boundary and a smoothed-boxcar function in the along-strike direction. The B functions of SUB steps have their maxima offset 55 km to the down-dip side of the fault trace, and this axis is drawn along the direction of relative plate motion. Spatial integral of each B function is unity.

for the six symmetric step classes, with a comparable but asymmetric formula for subduction zones (Fig. 2). The truncation of X_i at the apparent half-width h_k is necessary to honor the definition introduced in the previous section.

Local variable s expresses position along a horizontal axis parallel to the step, with values of 0 and ℓ_i at its ends. Earthquakes actually caused by this step should only appear beyond the ends of the step due to step location error and/or earthquake location error, but not due to finite width of the plate boundary, or the effects of faults dipping away from the surface trace. These errors are not expected to exceed 65 km (compare sums of rows 3 and 4 in Table 1), which is much less than the half-width of any of the boundary classes.

Therefore, we assume a more rapid variation of Y along this axis: we use the product of two normal cumulative distribution functions to produce a "smoothed boxcar" function:

$$Y_i(s_i(\theta,\phi)) = c\left[\int_{-\infty}^{s} e^{-s'^2/2\sigma^2}\mathrm{d}s'\right]\left[\int_{s}^{\infty} e^{-(s'-l_i)^2/2\sigma^2}\mathrm{d}s'\right] \quad (5)$$

where $2\sigma = 65$ km, and c is computed so that $\int_{-\infty}^{\infty} Y_i(s)\mathrm{d}s = 1$.

Subscript $j = 1, \ldots, 5$ in (2) distinguishes among a set of (up to) five "model earthquakes" for each boundary class k, which are customized to the particular trace azimuth and relative plate velocity azimuth of step i. All model earthquakes are double-couple sources. C_{ij} is the relative probability of the different types of model earthquake, with $\sum_{j=1,5} C_{ij} = 1$. $D_{ij}(z,\theta,\phi)$ is the probability density that this type of model earthquake takes place at depth z, with $\int_0^{70\ \mathrm{km}} D_{ij}\mathrm{d}z = 1$.

Finally, $E_{ij}(\hat{\tilde{M}})$ is the probability density that normalized moment tensor $\hat{\tilde{M}}$ has the right mechanism to be model earthquake type j on step i. We approximate E as a function of a single scalar measure: the size of the minimum three-dimensional rotation Φ necessary to make the principal axes of the model earthquake and the actual earthquake coincide (Kagan, 1991b). We design E (Fig. 3) so that it is zero for rotations greater than a limiting angle Φ_m:

$$E(\Phi) = \frac{3}{2\Phi_m}\begin{cases} 1 - (\Phi/\Phi_m)^2; & \Phi \le \Phi_m \\ 0; & \Phi > \Phi_m \end{cases} \quad (6)$$

This guarantees that an actual earthquake will never be associated with a plate boundary on which it would imply the wrong sense of slip. If moment tensors were free from error, and the only reason for unexpected directions of moment tensor axes were the low friction of some faults, then one might choose Φ_m as 45°. However, Kagan (2003) compared paired moment tensors of shallow earthquakes from different catalogs and found a median relative rotation of 22°. This suggests that tensors in each catalog may be rotated from the true mechanisms by median amounts of about 15°. Therefore, we adopt a more permissive limit of $\Phi_m = 60°$.

When defining model earthquakes for each type of boundary step, it is important to consider the general case, in which the step is neither parallel nor perpendicular to the relative plate velocity. Then no single focal mechanism with a vertical principal axis can produce the necessary heave (horizontal component of slip) vector, so either oblique mechanisms or partitioned mechanisms are required (Fig. 4). For oblique mechanisms, we assume that the heave vector is parallel to relative plate velocity, but that fault strike is

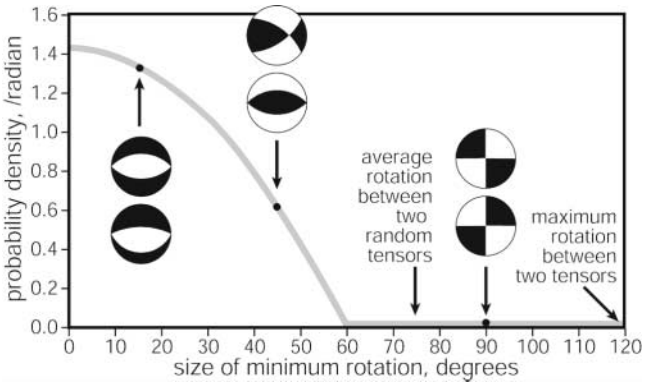

Figure 3. Angular PDF E (equation 6) associated with the minimum three-dimensional rotation angle that will transform an actual normalized double-couple moment tensor into that of a model earthquake. Pairs of focal mechanisms are shown to illustrate angular discrepancies of (left to right) 15°, 45°, and 90°. Small angular discrepancies are tolerated with little penalty in assigned probability, but discrepancies approaching 90° are not permitted, because in some cases this would imply that slip actually occurred in the "wrong" direction on the associated model fault plane. Earthquakes whose E is zero with respect to one model earthquake may still match a different model earthquake on the same boundary step, or a model earthquake of an adjacent plate-boundary step. If no possible match exists, they are assumed to be intraplate earthquakes.

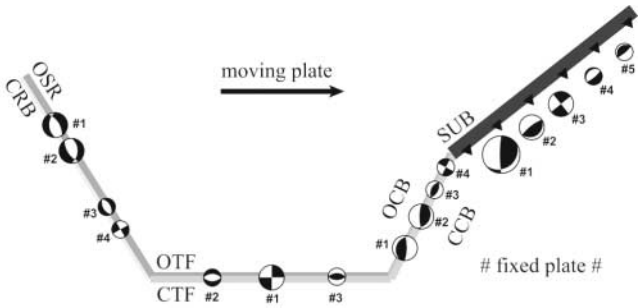

Figure 4. Enumeration of the model earthquakes associated with each kind of plate-boundary step. Several distinct mechanisms can be produced along a boundary step that is neither parallel nor orthogonal to relative plate velocity. Slip can be partitioned between pure strike slip and pure dip slip on faults of vertical and lesser dip (sharing the same trace and strike), or slip can be oblique on a single dipping fault. In CRB, OSR, OCB, and CCB steps, the sense of dip of the fault(s) is not known, giving two distinct possible mechanisms in the cases of oblique slip. In cases of partitioned dip slip, we approximate all possible normal (or thrust) faults by a generic normal (or thrust) mechanism with nodal planes dipping 45° each way. Because of the tolerance allowed by the E function (Fig. 3), possible dip variations of ± 20° will not significantly affect the estimated probabilities of a match between actual and model mechanisms.

parallel to the plate-boundary step. If the sense of dip of the boundary fault is unknown (CRB, CCB, OSR, OCB) then two oblique mechanisms could occur. Another possibility is that slip is partitioned into pure strike slip and pure dip slip on faults of vertical and lesser dip, respectively, that strike parallel to the step. In cases of partitioned dip slip, we approximate all possible normal (or thrust) faults by a generic normal (or thrust) mechanism with nodal planes dipping 45° each way. Because of the tolerance allowed by the E function (Fig. 3), possible dip variations of $\pm 20°$ will not significantly affect the estimated probabilities of a match between actual and model mechanisms.

For an extensional boundary step (CRB or OSR) model earthquakes 1 and 2 have oblique slip on planes dipping 55° to either side of the fault trace. There is an alternative possibility of slip partitioning between purely dip-slip normal faults (earthquake 3) and vertical strike-slip faults (earthquake 4). The probability of the partitioned strike-slip model is assumed proportional to the cosine of the angle between boundary and relative plate-velocity azimuths, whereas the remaining probability is divided equally among the normal-faulting models 1–3.

For nominally strike-slip plate boundaries (CTF and OTF) there are three model earthquakes. Primary model 1 is strike slip on a vertical plane. Model events 2 and 3 are normal and thrust events, respectively, on other faults striking parallel to the transform, which accommodate extensional or compressional components of relative velocity. Model PB2002 is not accurate enough to predict the sense of these components, so we include both dip-slip model earthquakes for each transform. However, because model PB2002 restricts the designation CTF and OTF to boundaries within 20° of the relative plate-velocity azimuth, we expect the mean rate of transform-normal strain to be less than 17% of transform-parallel strain, and set $C_{i2} = C_{i3} = 0.085$.

For a convergent boundary step (CCB or OCB) model earthquakes 1 and 2 have oblique slip on planes dipping 20° to either side of the fault trace. It is also possible that slip is partitioned into pure thrusting (earthquake 3) and pure strike slip (earthquake 4) on faults of different dip that strike parallel to the boundary. Again, the probability of the strike-slip model is assumed proportional to the cosine of the angle between boundary and relative plate-velocity azimuths, whereas the remaining probability is divided equally among the other three models.

For subduction zones (SUB), the five model earthquakes are: (1) oblique slip on the main interplate thrust fault, with heave parallel to relative plate velocity and slip plunging gently toward the volcanic arc (according to a quadratic model of the depth to the top of the slab); (2) pure dip slip on the interplate thrust fault (due to partitioning); (3) slip parallel to the trench on a vertical strike-slip fault striking parallel to the trench (also due to partitioning); (4), down-dip extension due to plane-strain bending within the subducting slab, usually (but not always) in the upper half of the double seismic zone; and (5) down-dip compression due to plane-strain bending within the subducting slab, usually (but not always) in the lower half of the double seismic zone.

The depth functions $D_{ij}(z,\theta,\phi)$ are used to express our *a priori* knowledge of the likely depths of these model earthquakes. With two exceptions, they are based on a normal cumulative distribution,

$$D_{ij}(z,\theta,\phi) \sim \int_{z}^{\infty} e^{-(z' - d_{ij}(\theta,\phi))^2/2\Delta_{jk}^2} \mathrm{d}z', \tag{7}$$

for earthquakes expected to be above $d_{ij}(\theta,\phi)$, or,

$$D_{ij}(z,\theta,\phi) \sim \int_{-\infty}^{z} e^{-(z' - d_{ij}(\theta,\phi))^2/2\Delta_{jk}^2} \mathrm{d}z', \tag{8}$$

for earthquakes expected to be below $d_{ij}(\theta,\phi)$, where $d_{ij}(\theta,\phi)$ is the cutoff depth, and Δ_{jk} is the combined uncertainty in cutoff depth and earthquake depth. For all model earthquakes on all non-SUB steps, we use a uniform d of 25 km (as the maximum depth) and Δ of 15 km (Fig. 5). The same function applies to model earthquake 3 of subduction zones (partitioned strike slip in the arc). However, plate-bending model earthquakes (nos. 4 and 5) in SUB steps have minimum expected depths that vary spatially in accord with the model depth of the subducting slab. The depth function D for interplate thrust earthquakes (nos. 1 and 2) in SUB steps is a Gaussian probable density function (PDF) centered on the model depth of the top of the slab. As in the design of SUB model earthquakes, the depth to the top of the slab is assumed to be a quadratic function of distance from the trench, with its own standard error of 10%. Although these rules add complexity to the classification process, we have found them to be necessary to prevent large normal-faulting earthquakes located at 40- to 70-km depths (probably occurring in subducting slabs) from being associated with backarc-spreading centers (OSR and CRB) that overlie many subduction zones.

Each seismic catalog has events for which the depth could only be constrained as "shallow." In the Harvard CMT catalog, these events are listed at the traditional NEIC default depth of 33 km (G. Ekström, personal comm., 2002). In the Pacheco and Sykes (1992) catalog, these events (about half) are listed with depths of 0 km. In these situations, we omit the depth factor D.

Another problem with the early instrumental record (1900–1975) from the Pacheco and Sykes (1992) catalog is that full moment tensors are not available. Some earthquakes have a generic mechanism (such as "thrust" or "normal") and in these cases we simplify the E term to a binary choice of 0 (when the model earthquake and actual earthquake are of different generic types) or 1 (when they are the same generic type). When no mechanism information is available,

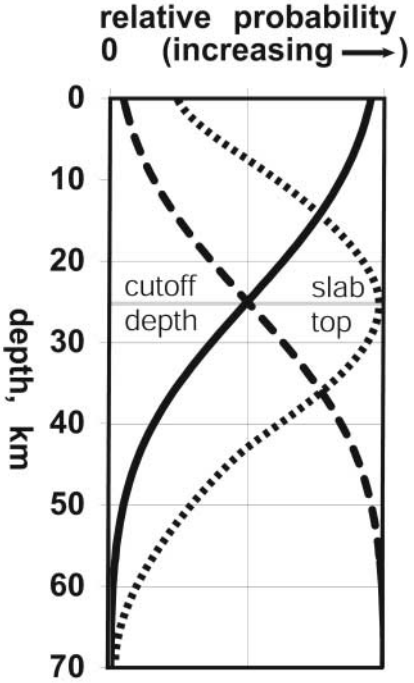

Figure 5. Depth PDFs D associated with model earthquakes. Most are based on integrated normal distributions, reflecting the hypothesis that the earthquake is above (solid line), or below (dashed line), a cutoff depth. Only slab-interior model earthquakes in subduction zones have a minimum depth (at the top of the slab, whose depth varies spatially). Most other model earthquakes have a fixed maximum depth. The depth PDF for intraplate-thrusting model earthquakes in SUB steps (dotted curve) is based on a normal distribution centered on the estimated depth of the top of the slab, which for purposes of this figure is also taken as 25 km, but which varies spatially in actual classification. The smoothness of these D functions is appropriate because both actual earthquake depths and model cutoff (or slab-top) depths contain errors.

we simply omit the mechanism factor E. These inconsistencies in relative-probability formulas between earthquakes do not cause any problems because we only compare relative probabilities of different plate-boundary steps for one earthquake; we never compare relative probabilities between different earthquakes.

Results

Maximum-Probability Subcatalogs. To establish the relative seismicities of the different boundary classes (N_k), this algorithm was run repeatedly on 5244 shallow ($z \leq 70$ km) earthquakes from the Harvard CMT catalog (1 January 1977 to 30 September 2002) above $M_t = 3.5 \times 10^{17}$ N m ($m_t \cong 5.66$). This part of the catalog is believed to be complete (Bird *et al.,* 2002; Kagan, 2003). After five iterations, the results (excluding orogens) were the following: CRB 134 (3%), CTF 198 (5%), CCB 274 (7%), OSR 142 (4%), OTF 838 (21%), OCB 105 (3%), SUB 2049 (52%), and INT 199 (5%). The designation of 5% of nonorogenic shallow earthquakes as intraplate is consistent with the way in which the apparent half-widths were chosen in the preceding section.

These figures are global totals, from boundary classes that have different net lengths and different mean rates. It is interesting to know relative seismicity levels for common length and relative plate velocity. We make a reasonable assumption that seismicity within most boundary classes is proportional to relative plate velocity. Preliminary results of Bird *et al.* (2000) showed that this appears to be true in SUB and CTF boundaries. Kreemer *et al.* (2002) demonstrated linearity for SUB boundaries. However, Bird *et al.* (2002) showed that OSR boundaries have something like an inverse dependence. To minimize confusion due to this effect, we scale seismicity of other classes to 48 mm/a, which is the mean rate of OSR boundaries. Note that this is 20% higher than the length-weighted mean velocity of all plate boundaries worldwide (39.6 mm/a; Bird, 2003).

These scaled rates are presented in Table 2. The highest and lowest rates differ by a factor of CCB/OSR = 25, which confirms our basic assumption that it is valuable to divide earthquakes by plate-boundary class. The only case where it might appear that we have introduced an unnecessary distinction is CTF/OTF, for which the rate ratio is 1.01. However, we shall see that these classes have different seismicities at higher thresholds.

In preparation for the classification of the Pacheco and Sykes (1992) catalog ($M_s \geq 7$), we also determine the relative seismicity factors N_k from earthquakes in the Harvard CMT catalog at a similar threshold of $M_t = 3.5 \times 10^{19}$ N m ($m_t \cong 6.99$). We use the 224 largest shallow events from CMT (1 January 1977 to 30 September 2002), augmented by the 15 largest shallow events from the 1976 catalog of Ekström and Nettles (1997). After three iterations, the converged results (excluding orogens) are the following: CRB 4 (3%), CTF 9 (6%), CCB 10 (6%), OSR 1 (1%), OTF 6 (4%), OCB 10 (6%), SUB 111 (71%), and INT 6 (4%). Although these counts are small and therefore less reliable, it appears that the proportion of OSR and OTF events has dropped, the proportion of OCB and SUB events has risen, and the other four classes retain their former proportions.

When we analyze the 1900–1975 portion of the Pacheco and Sykes (1992) catalog with these N_k values, the results (excluding orogens) are the following: CRB 8 (2%), CTF 34 (8%), CCB 27 (7%), OSR 1 (0%), OTF 15 (4%), OCB 22 (5%), SUB 275 (68%), and INT 21 (5%). Although these are slightly different from the 1976–2002 values, we do not perform any iteration. This is because we consider the modern catalog, with its moment tensors and consistently accurate locations, to be a better basis for estimating relative seismicity levels N_k than the early instrumental catalog, even though the early catalog is three times longer. In fact, three erroneous results were noted in this classification set: the Tokyo (or Kwanto) earthquake of 1 September 1923 was classified as a CCB event associated with the Japan Alps, but the pattern of uplift and lack of subaerial ground breakage

showed that it was a SUB event. The 11 November 1922 tsunamigenic Chile earthquake and the 28 March 1964 Alaska earthquake, also known to be SUB events, were classified as INT/orogen because poor locations and/or unusually wide forearcs caused them to fall too far from their associated trenches. These misclassifications were corrected manually. Presumably, there were additional undetected misclassifications of earthquakes that are less famous.

Monte Carlo Subcatalogs. Five alternative sets of Monte Carlo subcatalogs were also computed, to permit testing of the sensitivity of all our results to residual uncertainties in classification (as explained in Algorithms). When computing multiple realizations of the Monte Carlo classification of a catalog, we use iteration to represent the effects of the stochastic uncertainty in the N_k values. Classification is started by using N_k from the maximum-probability results quoted above and continued for five iterations to allow the N_k to adjust to the Monte Carlo classification rule. Then, an additional five iterations were recorded, giving five complete sets of subcatalogs, to give a rough measure of the new stochastic equilibrium and its variations.

With the shallow complete part of the CMT catalog (1 January 1977 to 30 September 2002, $z \leq 70$ km, $M_t = 3.5 \times 10^{17}$ N m, $m_t \cong 5.66$) the range of results in these latter five iterations was (excluding orogens): CRB, 136–150 (3%–4%); CTF, 195–209 (5%); CCB, 229–249 (6%); OSR, 150–158 (4%); OTF, 809–827 (21%); OCB, 122–141 (3%–4%); SUB, 2037–2065 (52%); INT, 199 (5%). The most noticeable change is that the CCB count is lower by 25–45 events and OCB is higher by 17–36. Apparently events have been transferred between these two categories along plate boundaries that are consistently convergent but that alternate between "oceanic" and "continental" classification because of variations in water depth.

With the moment tensor catalog of large earthquakes ($M_t = 3.5 \times 10^{19}$ N m, $m_t \cong 6.99$, *Ekström and Nettles* (1997) catalog for 1976 plus CMT 1 January 1977 to 30 September 2002) the range of results in these latter five iterations was (excluding orogens): CRB, 3–5 (2%–3%); CTF, 6–11 (4%–7%); CCB, 10–12 (6%–8%); OSR, 1 (1%); OTF, 6–8 (4%–5%), OCB, 8–20 (5%–13%); SUB, 109–112 (69%–71%); INT, 6 (4%). All ranges include the previous maximum-probability results.

As before, we classified the 1900–1975 portion of the *Pacheco and Sykes* (1992) catalog with the N_k values from the preceding paragraph (including their random variations over five iterations), rather than using self-consistent empirical values. The range of results (excluding orogens) was: CRB, 6–12 (1%–3%); CTF, 29–39 (7%–10%); CCB, 24–28 (6%–7%); OSR, 1–2 (0%); OTF, 13–20 (3%–5%); OCB, 24–26 (6%); SUB, 265–272 (66%–67%); INT, 21 (5%). Most ranges include the previous maximum-probability result, except that class OCB has 2–4 more and class SUB has 4–11 fewer.

All subcatalogs discussed in this article are shown in an electronic supplement (Ⓔ available online at the SSA Web site). Plots of log-cumulative-number versus magnitude can also be found there for each of the maximum-probability subcatalogs.

Tapered Gutenberg-Richter Distributions

To obtain the long-term-average moment rate for each class of plate boundary, it is not enough to sum the moments of earthquakes in each subcatalog. This gives unstable results because so much of the moment resides in the largest earthquake (McCaffrey, 1997; Holt *et al.,* 2000). Also, it misses the contributions to moment rate of very large but very rare earthquakes, as well as the contribution of earthquakes too small to be detected by the network. Therefore, we prefer to fit a model frequency/moment distribution to each subcatalog and then integrate the model moment rate over all moments.

In this study we use the tapered Gutenberg-Richter distribution (Jackson and Kagan, 1999, Kagan and Jackson, 2000), defined by

$$G(M,M_t,\beta,M_c) = \left(\frac{M}{M_t}\right)^{-\beta} \exp\left(\frac{M_t - M}{M_c}\right), \qquad (9)$$

where G is the fraction of earthquakes (by event count) in the catalog with moment exceeding M, M_t is the threshold moment for completeness of the catalog, β is the asymptotic spectral slope at small moments, and M_c is the corner moment. The exponential term involving the corner moment guarantees that this distribution of moments has a finite integral for $\beta < 1$. Using (1), there is a corner magnitude m_c associated with M_c, and a threshold magnitude m_t associated with M_t. In log-frequency/magnitude plots it is natural to compare $3\beta/2$ with the traditional Gutenberg-Richter slope parameter b. However, it should be remembered that b is defined as the mean slope in the accessible magnitude range, whereas $3\beta/2$ is defined as the asymptotic slope at magnitudes much less than m_c.

As in many previous studies (since Kagan, 1991a), we use the maximum-likelihood method to estimate the parameters β and M_c (or m_c) for each subcatalog. We compute the log-likelihood function ℓ, which is the natural logarithm of the likelihood that the given catalog would be observed if the current trial values of β and M_c were correct, under the constraint of fixed catalog size. For the tapered Gutenberg-Richter distribution,

$$l = N\beta \ln(M_t) + \frac{1}{M_c}\left(NM_t - \sum_{i=1}^{N} M_i\right) - \beta\sum_{i=1}^{N} \ln(M_i) + \sum_{i=1}^{N} \ln\left(\frac{\beta}{M_i} + \frac{1}{M_c}\right) \qquad (10)$$

(Kagan and Jackson, 2000; Kagan, 2002a), where N is the

number of earthquakes in the catalog with $M_i > M_t$. This function is evaluated for many points on a grid of (β, M_c) values, which has linear variation along the β axis and logarithmic variation along the M_c axis (or linear variation along the associated m_c axis). The highest log-likelihood is designated as ℓ_{max}; the associated values (β, M_c or m_c) are the maximum-likelihood estimates of these parameters (Fig. 6). For large N, the absolute value of the error in either parameter has the distribution known as χ^2_2 (chi-squared with 2 degrees of freedom) with respect to an independent variable defined as $w \equiv 2(\ell_{max} - \ell)$. Therefore, the 95% confidence limits on the parameters can be found along the contour $w = 5.99$, corresponding to $\ell = \ell_{max} - 2.995$. For convenience, we add a constant to all values of ℓ in each plot to adjust ℓ_{max} to the value $+3$, so that the zero contour is approximately the 95% confidence limit.

If the subcatalog is large, is homogeneous, includes earthquakes near or above the corner moment, and has an M_c/M_t ratio of 100 or more, the limiting contour typically has an elliptical form, with both parameters well determined (Fig. 6G, H). If the M_c/M_t ratio is less, the ellipse of good solutions is replaced by a curved diagonal swath, expressing a trade-off between β and M_c (Fig. 6D). This happens when the range of earthquake moments is insufficient to define the curvature of the log-frequency/log-moment relation. If the subcatalog lacks sufficient large earthquakes, the plot may have a zero contour that is open to infinity in the positive M_c direction (Fig. 6A, B, C, E, F, I). This is because trial M_c values much larger than the largest M_i in the subcatalog all result in straight-line (Gutenberg-Richter) distribution models in the range $M_t < M \leq \sup(M_i)$, and such models are indistinguishable from one another. In tables, we use a

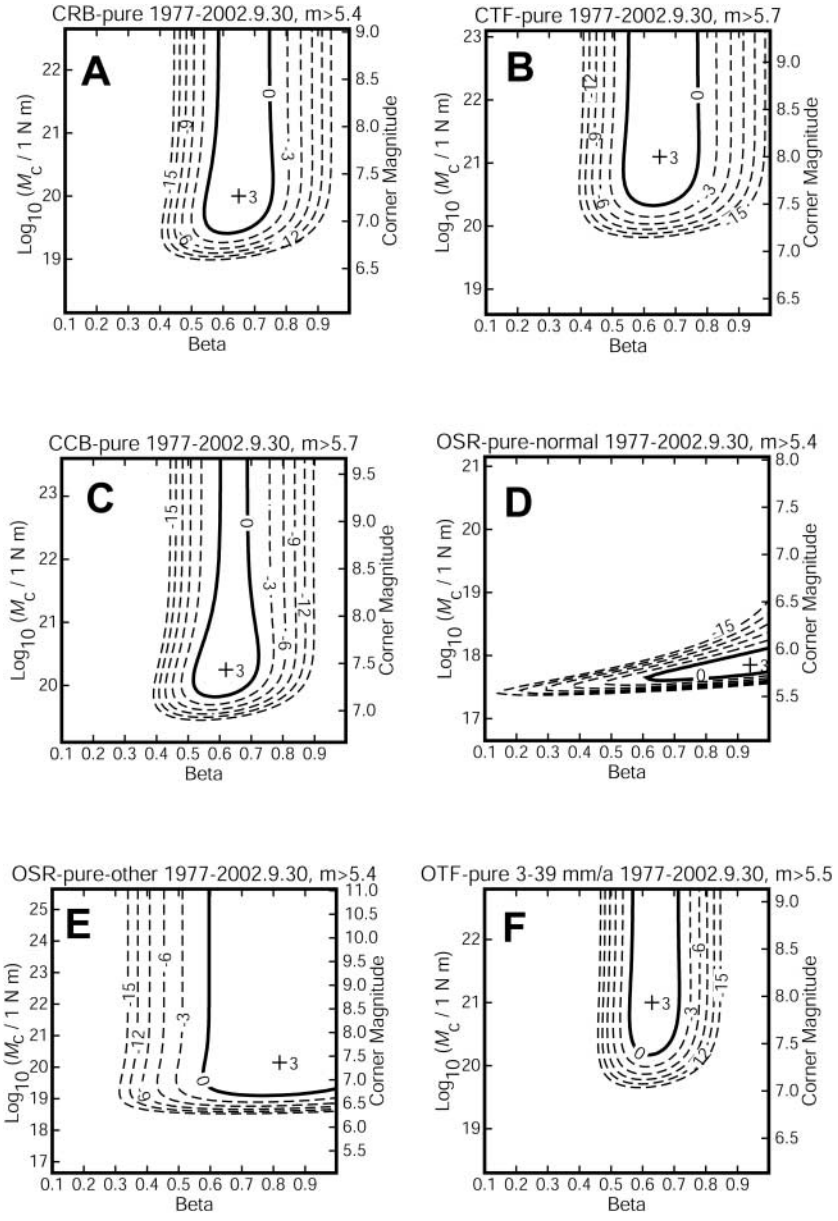

Figure 6. (*Caption on next page.*)

query (?) to indicate that an upper limit for the corner magnitude was not found.

Because the analysis of the CMT catalog (excluding orogens) frequently cannot determine an upper bound on corner magnitude, we also analyzed subcatalogs that were extended in two ways. First, we formed "merged" subcatalogs of large earthquakes for 1 January 1900 to 30 September 2002 by combining the 1900–1975 portions of the subcatalogs from Pacheco and Sykes (1992) with the large earthquakes ($M_t = 3.5 \times 10^{19}$ N m, $m_t \cong 6.99$) from the 1976 subcatalogs derived from Ekström and Nettles (1997) and from the CMT subcatalogs. Second, we included earthquakes from plate-boundary steps lying within orogens. (This includes the thrust earthquakes of the Himalayan front and the 28 March 1964 Alaska earthquake, for example. Inclusion of orogens is indicated by keyword "all" instead of keyword "pure" in file names in the electronic supplement [Ⓔ available online at the SSA Web site].) Analyzing these merged subcatalogs (Fig. 7), we find that the β values are much more uncertain than those obtained from the CMT catalog because of the smaller M_c/M_t ratio and some problems of completeness and consistency in the early instrumental record. Therefore, we fix β at the 1977–2002 CMT value, and redefine ℓ_{max} as the highest log-likelihood occurring in that column of the log-likelihood grid, and define the associated M_c as the constrained maximum-likelihood estimate of corner moment. In this conditional case, the maximum-likelihood estimation is for a single parameter, so the absolute value of the error in the parameter has the distribution known as χ_1^2 (chi-squared with 1 degree of freedom) with respect to $w \equiv 2(\ell_{max} - \ell)$. Therefore, the 95% confidence limits on the parameter can be found at the two points where $w = 3.84$ and $\ell = \ell_{max} - 1.92$.

These merged catalogs show a stair-step pattern in their log-frequency/magnitude distributions with period 0.1 magnitude units, which results from prior rounding of surface-wave magnitudes to the nearest multiple of 0.1 by early researchers. To minimize any effects this might have on model distributions that we fit in this article, we adopt a moment threshold of $M_t = 5.1 \times 10^{19}$ N m ($m_t \cong 7.10$), which is actually centered between two steps. This slightly higher threshold also allows for the possibility of threshold inflation during conversion of magnitude scales. Tests showed that varying this threshold magnitude by $\pm$ 0.05 in steps of 0.01 does not change resulting corner magnitudes (at fixed β) by more than 0.02 (large subcatalogs) to 0.05 (small subcatalogs).

Results from these maximum-likelihood analyses will be discussed in the next paragraphs. Results from analyses of the CMT and merged maximum-probability subcatalogs are summarized in Table 3. Mean results from the five sets of Monte Carlo subcatalogs are shown in Table 4. In general, these are similar to the maximum-probability results; one exception will be noted in the OTF category. All uncertainties quoted are 95% confidence limits.

CRB. Continental Rift Boundaries include the East Africa rift, Baikal rift, and Okinawa Trough, and less famous submarine rifts (with water depth $<$ 2000 m) in the Aru Trough

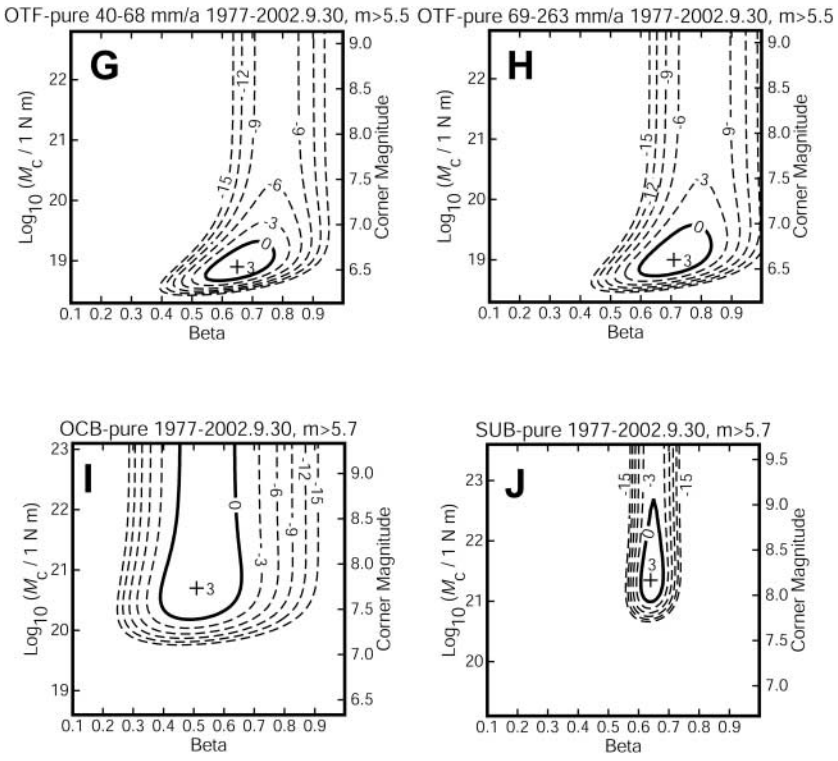

Figure 6. Contour maps of relative log-likelihood, showing preferred value (at peak, +3) and 95% confidence interval (within zero contour) of the parameters β and M_c (or m_c) of tapered Gutenberg-Richter frequency/moment distributions fit to maximum-probability subcatalogs derived from nonorogen regions and the Harvard CMT catalog (1 January 1977 to 30 September 2002; called "CMT pure" subcatalogs): (A) CRB; (B) CTF; (C) CCB; (D) OSR/normal faulting; (E) OSR/other mechanisms; (F) OTF/3–39 mm/a; (G) OTF/40–68 mm/a; (H) OTF/69–263 mm/a; (I) OCB; (J) SUB. Compare with upper part of Table 3, which lists threshold moments.

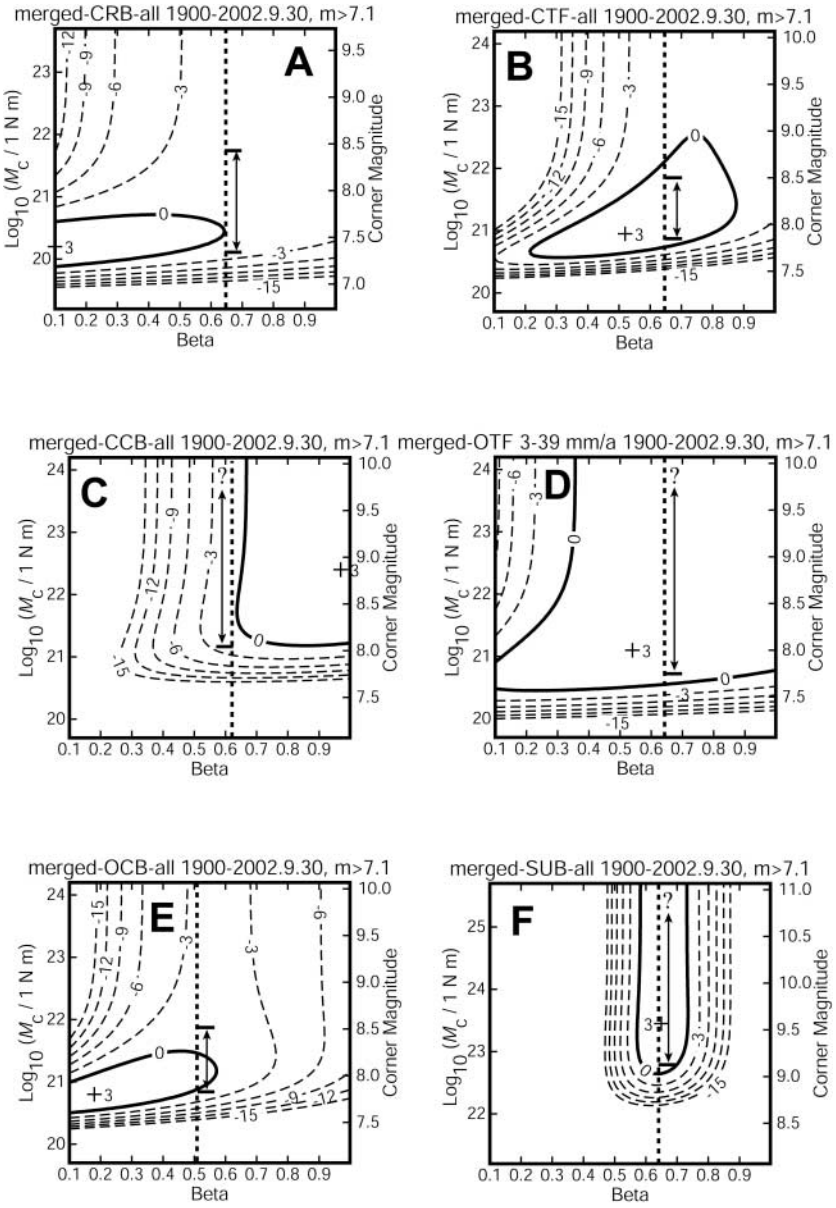

Figure 7. Contour maps of relative log-likelihood for tapered Gutenberg-Richter frequency/moment distributions fit to maximum-probability "merged" subcatalogs of the merged (1 January 1900 to 30 September 2002) catalog of large ($M > 5.1 \times 10^{19}$ N m) shallow earthquakes: (A) CRB; (B) CTF; (C) CCB; (D) OTF/3–39 mm/a; (E) OCB; (F) SUB. Format as in Figure 6. Compare with lower part of Table 3, which lists threshold moments. These subcatalogs include orogen regions and the years 1900–1976. The threshold magnitude is higher than in Figure 6, making it difficult to resolve β in most cases. Vertical dotted lines indicate the best estimate of β from the CMT subcatalogs (excluding orogens) in Figure 6, and corner magnitude is inferred from relative log-likelihood values along this line, with 95% confidence ranges shown by the double-headed arrows.

and parts of the Lau-Havre Trough. We believe the CMT subcatalog to be complete above $M_t = 1.13 \times 10^{17}$ N m ($m_t \cong 5.33$) (Kagan, 2003); this gives 286 events. The zero contour of the log-likelihood plot (Fig. 6A) is open toward large corner magnitudes, so an upper limit is lacking ($m_c = 7.3^{+?}_{-0.4}$). When we form merged 1900–2002 subcatalogs of $m > 7.10$ CRB events, they are very small (9–17 events) because the threshold is now almost equal to the corner magnitude. Nevertheless, by assuming the modern CMT value of $\beta = 0.65$. (Fig. 7A), we can extract weak upper limits on corner magnitude: $m_c = 7.60^{+0.82}_{-0.26}$ from the maximum-probability subcatalog, and $m_c = 7.68^{+0.72}_{-0.25}$ from the mean of results from the five Monte Carlo subcatalogs.

CTF. Well-known Continental Transform Faults include the North Anatolia fault, Quetta fault,* Sagaing fault,* Alpine fault, San Andreas fault,* and Bocono fault. (*These faults are in orogens.) However, about half of the total fault length and seismicity comes from short, mostly submarine faults in the western Pacific margins. CMT seismicity which falls in the CTF subcatalog (excluding orogens) has a nearly straight-line log-frequency/magnitude distribution, so maximum-likelihood analysis gives well-constrained $\beta = 0.65 \pm 0.12$ but incomplete information on the corner magnitude (>7.52, estimate 8.02, Fig. 6B). Assuming that the same β applies to the merged subcatalog of all large CTF earthquakes in 1900–2002 ($52 > M_t = 5.1 \times 10^{19}$ N m), we obtain a constrained corner magnitude of $8.03^{+0.47}_{-0.22}$ (Fig. 7B), which agrees with the CMT estimate. The four largest CTF events in the Pacheco and Sykes (1992) catalog have moments from the literature, so scaling from surface-wave magnitudes is unlikely to have biased this estimate.

Table 3
Tapered Gutenberg-Richter Frequency-Magnitude Parameters of Maximum-Probability Subcatalogs

	Class									
	CRB Continental Rift Boundary	CTF Continental Transform Fault	CCB Continental Convergent Boundary	OSR Oceanic Spreading Ridge		OTF Oceanic Transform Fault, by Plate Velocity, (mm/a)			OCB Oceanic Convergent Boundary	SUB SUB-duction Zone
Catalogs				Normal	Other	3–39	40–68	69–263		
Harvard CMT Catalog (01/01/77–09/30/02)										
Threshold, M_t, N m	1.13×10^{17}	3.5×10^{17}	3.5×10^{17}	1.13×10^{17}		2×10^{17}			3.5×10^{17}	
All earthquakes*	353*	272*	357*	458*	77*	428*	447*	416*	119*	2723*
Excluding orogens	286	198	274	422	64	400	413	385	105	2049
Slope, β	0.65	0.65	0.62	0.93	0.82	0.64	0.65	0.71	0.51	0.64
	±0.11	±0.12	±0.10	0.61–1	0.58–1	±0.08	±0.11	±0.11	0.39–0.66	±0.04
Corner magnitude, m_c	7.30	8.02	7.48	5.87	7.40	7.98	6.57	6.63	7.77	8.20
	6.90–?	7.52–?	7.18–?	5.7–6.04	6.68–?	7.42–?	6.4–6.84	6.46–7.01	7.42–?	7.96–9.10
Pacheco and Sykes [1992] catalog (1900–1975) and *Ekström and Nettles* [1997] catalog (1976): $M_s \geq 7$										
Threshold, M_t, N m	5.1×10^{19}									
All earthquakes*	10*	42*	32*	1*		7*	1*	3*	21*	275*
Excluding orogens	9	30	19	1		7	1	3	18	218
Three catalogs merged (1900–2002): $M_s \geq 7$										
Threshold, M_t, N m	5.1×10^{19}									
All earthquakes*	11*	51*	45*			11*			28*	389*
Slope, β	0.65†	0.65†	0.62†			0.64†			0.51†	0.64†
Corner magnitude, m_c	7.60*	8.03*	8.43*			8.12*			8.03*	9.58*
	7.34–8.42	7.81–8.50	8.03–?			7.73–?			7.82–8.51	9.12–?

*Including earthquakes in the 13 orogens.
†From CMT results.
All ranges are 95% confidence limits.

Table 4
Tapered Gutenberg-Richter Frequency-Magnitude Parameters from Mean of Five Sets of Monte Carlo Subcatalogs

	Class									
	CRB Continental Rift Boundary	CTF Continental Transform Fault	CCB Continental Convergent Boundary	OSR Oceanic Spreading Ridge		OTF Oceanic Transform Fault, by Plate Velocity, (mm/a)			OCB Oceanic Convergent Boundary	SUB SUB-duction Zone
Catalogs				Normal	Other	3–39	40–68	69–263		
Harvard CMT catalog (01/01/77–09/30/02)										
Threshold, M_t, N m	1.13×10^{17}	3.5×10^{17}	3.5×10^{17}	1.13×10^{17}		2×10^{17}			3.5×10^{17}	
All earthquakes*	347.2*	280.6*	320.4*	463.8*	104.6*	421.6*	431.8*	398.2*	148.0*	2733.4*
Excluding orogens	285.8	199.0	244.8	426.6	88.2	396.0	400.8	368.2	130.4	2056.6
Slope, β	0.64	0.64	0.61	0.91	0.82	0.63	0.64	0.76	0.54	0.64
	±0.10	±0.12	±0.10	0.59–1	0.61–1	±0.08	±0.11	±0.11	±0.13	±0.04
Corner Magnitude, m_c	7.44	8.01	7.48	5.85	7.38	7.97	6.53	7.14	7.77	8.21
	7.02–?	7.50–?	7.18–?	5.7–6.05	6.71–?	7.42–?	6.37–6.79	6.76–?	7.41–?	7.97–9.10
Pacheco and Sykes [1992] catalog (1900–1975) and *Ekström and Nettles* [1997] catalog (1976): $M_s \geq 7$										
Threshold, M_t, N m	5.1×10^{19}									
All earthquakes*	12.8*	39.6*	31.4*	1.6*		5.2*	3.4*	4.4*	21.8*	272.0*
Excluding orogens	10.0	30.6	19.2	1.6		5.2	3.4	4.2	19.2	214.2
Three catalogs merged (1900–2002): $M_s \geq 7$										
Threshold, M_t, N m	5.1×10^{19}									
All earthquakes*	14.2*	49.6*	44.2*			7.8*			29.6*	384.0*
Slope, β	0.64†	0.64†	0.61†			0.63†			0.54†	0.64†
Corner magnitude, m_c	7.68*	7.99*	8.50*			8.16*			8.06*	9.58*
	7.43–8.40	7.78–8.46	8.12–?			7.72–?			7.82–8.62	9.13–?

*Including earthquakes in the 13 orogens.
†From CMT results.
All ranges are 95% confidence limits.

CCB. About 46% of the total length of Continental Convergent Boundaries lies in orogens, especially the Alpine-Himalayan chain. Nonorogen CCB events are concentrated in southern Central America and northern South America, in the Japan Sea, around Taiwan, and around New Guinea. This subcatalog (excluding orogens) is large enough (274 events $> M_t = 3.5 \times 10^{17}$ N m / $m_t \cong 5.66$ by maximum probability) to give a well-constrained $\beta = 0.62 \pm 0.10$, and a best estimate of corner magnitude as 7.48 (>7.18), but because the zero contour does not close (Fig. 6C), there is no upper limit. When we analyze the merged catalog for 1900–2002, including orogens, its small size (45 events $> M_t = 5.1 \times 10^{19}$ N m / $m_t \cong 7.10$) and nonideal frequency/moment distribution led to a very broad log-likelihood maximum (Fig. 7C), and it is essential that we constrain β at the modern value. Then the corner magnitude is 8.43 (>8.03; no upper limit); this result would have been ~0.5 lower without the Assam earthquake of 15 August 1950, $m = 8.62$. (Although the five largest events in this subcatalog are all from the Pacheco and Sykes [1992] catalog, only one moment was scaled from surface-wave magnitude, and the moment of the critical Assam event was supported by three studies from the literature.) We will use this larger corner magnitude in further analysis, because it is based on four times as many years of experience and twice the geographic area of the CMT result.

OSR. In a previous article (Bird *et al.*, 2002), we studied normal-faulting earthquakes within 63.7 km of the mid-Ocean Spreading Ridges of plate model PB1999. We found that they have a very low corner magnitude of 5.8 and exhibit seismic coupling that decreases quasi-exponentially with relative plate velocity. This study enlarges the data set by: (1) using plate model PB2002, which has 27% more length of OSR boundaries; (2) incorporating 17% more years of the CMT record, (3) allowing some earthquakes with other focal mechanisms to be associated with OSR boundaries (+15%~22%), and (4) using 132 km as the apparent half-width.

The greatest change comes from the third factor, permitting other focal mechanisms. In the maximum-probability CMT subcatalog the three largest events have strike-slip mechanisms, and their magnitudes are so much larger than the largest normal-faulting events (by +0.5 to +1.5) that they produce a composite log-frequency/magnitude curve that is concave upward. This cannot be well fit by a tapered Gutenberg-Richter distribution, and if a fit is forced the result is $\beta \geq 1$, which is dubious because the integrated moment would diverge for $M \to 0$. Therefore, we have chosen to separate all OSR subcatalogs derived from CMT into "normal-faulting" subcatalogs (comparable with those of Bird *et al.,* 2002) and subcatalogs of "other" mechanisms (overwhelmingly strike slip). The normal-faulting results (Fig. 6D, Tables 3 and 4) are then very similar to what we found before: for example, for the maximum-probability subcatalog, $m_c = 5.87 \pm 0.17$ and $\beta = 0.93^{+0.07}_{-0.32}$. (The large uncertainty in β is caused by the corner magnitude lying so close to the threshold $m_t = 5.33$.) Results on "other" focal mechanisms (among which the 22 largest events are strike slip) are inconclusive, except that $\beta > 0.58$ and $m_c > 6.68$. Therefore, the corner magnitude for OSR strike-slip events is definitely higher than that for normal faulting.

Since the OSR subcatalogs formed from the 1900–1975 portion of the Pacheco and Sykes (1992) catalog have only one to two events (and these have unknown focal mechanisms), we have not studied any merged twentieth-century subcatalogs for OSR boundaries.

OTF. In our previous article (Bird *et al.,* 2002) we analyzed CMT strike-slip earthquakes within 111 km of Oceanic Transform Fault boundaries in plate model PB1999. We found that corner magnitude decreases as relative plate velocity increases; by splitting the subcatalog into three approximately equal parts by plate velocity we found m_c = 7.06, 6.59, and 6.37 at 1–39 mm/a, 39–67 mm/a, and 67–152 mm/a, respectively. This study enlarges the data set by (1) using plate model PB2002, which has 8% more total length of OTF; (2) incorporating 17% more years of CMT records, (3) allowing some earthquakes of non-strike-slip focal mechanisms to be associated with OTFs; and (4) using 128 km as the apparent half-width. These changes would combine to yield 50% more OTF earthquakes (above $M_t = 2 \times 10^{17}$ N m / $m_t \cong 5.50$), except that now we exclude orogens from most analyses; still, there are 40% more than before. As before, we label all earthquakes with the relative plate velocity of their associated OTF steps, sort by velocity, and split the subcatalog into three roughly equal-sized parts, which now span 3–39 mm/a, 40–68 mm/a, and 69–263 mm/a, respectively.

In our previous study the large $m = 8.06$ earthquake of 23 May 1989 on the Macquarie Ridge was excluded because of doubt that it occurred on an OTF. But detailed seafloor mapping by Massell *et al.* (2000) showed that the region has Tertiary oceanic crust, so we now incorporate this event in the slow-OTF subcatalog. This earthquake is 0.87 magnitude units larger than the next in its class (which occurred 7 years earlier in the same vicinity) and 0.93 larger than the largest CMT/OTF earthquake on a midocean spreading ridge. Consequently, the corner magnitude increases to $7.98^{+?}_{-0.56}$ and becomes unbounded from above (Fig. 6F, Tables 3 and 4).

Results for the medium-velocity subcatalogs (Fig. 6G, Tables 3 and 4) are similar to those found in the previous study: $m_c = 6.57^{+0.27}_{-0.16}$ (maximum-probability subcatalog) or $m_c = 6.53^{+0.26}_{-0.16}$ (mean of five Monte Carlo subcatalogs).

Results for the high-velocity subcatalogs (Fig. 6H, Tables 3 and 4) depend on the classification scheme: $m_c = 6.63^{+0.38}_{-0.17}$ and $\beta = 0.71 \pm 0.11$ (maximum-probability subcatalog) or $m_c = 7.14^{+?}_{-0.38}$ and $\beta = 0.76 \pm 0.11$ (mean of five Monte Carlo subcatalogs). The difference arises because three of the five Monte Carlo subcatalogs contain an extra

large earthquake that chanced to be assigned to class OTF (instead of SUB or CCB) despite low composite OTF probability (4%–15%). In this case, it appears that the lower maximum-probability corner magnitude is the better choice.

When we classify and sort all 1900–1976 large OTF earthquakes, the maximum-probability result is that seven events (above $M_t = 5.1 \times 10^{19}$ N m / $m_t \cong 7.10$) are added to the slow OTF subcatalog, but only one is added to medium-velocity OTF and three to fast OTF. We omit any further analysis of the latter two subcatalogs because the information potentially added by a few events does not justify the risk of bias inherent in fitting only earthquakes larger than the corner magnitude, especially pre-1976 events with unknown mechanisms. However, the slow-OTF category is less subject to this bias because its corner magnitude is already known to exceed 7.10; it is also interesting because it includes the $m = 8.04$ earthquake of 10 November 1942 on the Southwest Indian Ridge. The result from this merged 1900–2002 slow-OTF subcatalog is $m_c = 8.12^{+?}_{-0.39}$ (Fig. 7D, Tables 3 and 4), which is still lacking an upper limit. (The third and fifth largest events in this subcatalog have moments scaled from surface-wave magnitudes by Pacheco and Sykes [1992].)

The continuous decline in corner magnitude with velocity that we interpreted in the previous study was probably incorrect. Instead, it now appears that medium and fast OTF boundaries may share a common corner magnitude of about 6.6, whereas slow OTF boundaries have a much higher corner magnitude of about 8.1. It is difficult to proceed further in studying this difference because it rests on such a small number (~6) of critical large earthquakes.

OCB. At 6.7% of total boundary length, Oceanic Convergent Boundaries are the least common type on Earth. Examples include the India-Australia plate boundary in the Indian Ocean, the Amur-Okhotsk boundary in the Japan Sea, the Banda Sea-Timor boundary north of Timor, the Caroline-North Bismark boundary north of New Guinea, and the Australia-Pacific boundary south from the Macquarie Ridge. Although the CMT OCB subcatalog (excluding orogens) is not large ($105 > M_t = 3.5 \times 10^{17}$ N m / $m_t \cong 5.66$ by maximum probability), it fits a tapered Gutenberg-Richter distribution reasonably well (Fig. 6I) with $\beta = 0.51^{+0.15}_{-0.12}$ and $m_c = 7.77^{+?}_{-0.36}$ (Table 3). As in other cases where an upper limit on corner magnitude is lacking, we also analyze the merged 1900–2002 subcatalog (including orogens) of large earthquakes, limiting the search to alternative corner magnitudes at fixed β (Fig. 7E) and find $m_c = 8.03^{+0.48}_{-0.21}$. Results from Monte Carlo subcatalogs are almost identical (Table 4), except that $\beta = 0.54 \pm 0.13$. (The five largest events in this subcatalog are from Pacheco and Sykes [1992], but all had moments directly determined rather than scaled from surface-wave magnitude.)

SUB. Because SUBduction zones generate 52% of shallow earthquakes (outside orogens) above $M = 3.5 \times 10^{17}$ N m ($m \cong 5.66$), and 71% of such earthquakes above $M = 3.5 \times 10^{19}$ N m ($m \cong 6.99$), these subcatalogs are large and could potentially be subdivided in various ways. However, our own previous studies (Bird *et al.,* 2000; Kagan, 2002b) based on preliminary versions of this subcatalog showed only one strong signal: dependence of seismicity on relative plate velocity. Once seismicity was normalized by velocity, it did not vary systematically with relative plate velocity, ratio of parallel to perpendicular velocity components, estimated characteristic earthquake size (Nishenko, 1991), the time since the last major earthquake (Nishenko, 1991), or probability of a future characteristic earthquake (Nishenko, 1991). Dependence on age of subducted seafloor was proposed by Ruff and Kanamori (1980), but this hypothesis was rejected by Pacheco *et al.* (1993). We do not find any compelling reason to subdivide subduction zones, because 95% of subduction zones have β values whose 95% confidence limits include a universal value (Kagan, 1999).

By using the maximum-probability subcatalog of shallow CMT earthquakes (outside orogens), maximum-likelihood estimates are $\beta = 0.64 \pm 0.04$ and $m_c = 8.20^{+0.90}_{-0.29}$. Asymptotic slope β is constrained very tightly (Fig. 6J) because of the large number of events and the wide moment window between $M_t = 3.5 \times 10^{17}$ N m ($m \cong 5.66$) and M_c. The mean results from five Monte Carlo subcatalogs are identical (Table 4). However, it often remarked (*e.g.,* Kagan, 2002a) that the era of the CMT catalog has yet to include a truly great earthquake like the 22 May 1960 Chile ($m = 9.64$) or 28 March 1964 Alaska ($m = 9.22$) events, and that 26 years may not be a sufficient sample of the behavior of SUB boundaries because of their apparently large M_c. Therefore, we give greater credence to the corner magnitude determined from the merged 1900–2002 subcatalog with $M_t = 5.1 \times 10^{19}$ N m ($m_t \cong 7.10$): $m_c = 9.58^{+?}_{-0.46}$ (Tables 3 and 4). (The five largest events in this subcatalog are from Pacheco and Sykes [1992], but all had moments directly determined rather than scaled from surface-wave magnitude.) The zero contour of relative log-likelihood is open toward larger corner magnitudes (Fig. 7F), so no upper limit can be determined from seismicity statistics alone.

Coupled Thickness and Seismic Coupling

The assumed relation between plate tectonics and seismicity is

$$\frac{1}{R}\lim_{\Delta t\to\infty}\frac{\sum M}{\Delta t} = \int\int c\mu \dot{s} \mathrm{d}a = \int c\mu \sqrt{v_p^2 + (v_o \sec\theta)^2}\, z \csc(\theta) \mathrm{d}L \quad (11)$$

where R is the moment-recording factor of the seismic network ($0 < R \leq 1$), M is seismic moment, t is time, c is seismic coupling (the fraction of frictional sliding that occurs

in earthquakes), μ is the elastic shear modulus, $\dot{s}$ is the long-term-average slip rate of a plate-boundary fault, a is the area of the fault with friction-dominated rheology, v_p is the parallel component of relative plate velocity, v_o is the orthogonal component, θ is the dip of the plate-boundary fault, z is the thickness of the seismogenic (friction-dominated part of the) lithosphere, and L is the length along the plate-boundary trace.

As explained in the previous section, we believe the best available estimate of the long-term moment rate is the integral of the best-fitting tapered Gutenberg-Richter distribution:

$$\frac{1}{R}\lim_{\Delta t\to\infty}\frac{\Sigma M}{\Delta t} \cong \frac{N{:}M > M_t}{\Delta t}\int_0^\infty M\,\frac{\partial G(M,M_t,\beta,M_c)}{\partial M}\,dM, \quad (12)$$

(where $N{:}\ M > M_t$ is the number of earthquakes with moment M greater than the threshold moment M_t) using the maximum-likelihood estimates of the parameters determined in the previous section. These integrals are shown in Table 5 (together with rates from simple moment sums). The N values, and therefore the integrals, are for nonorogen regions only and have been further subdivided according to the seven plate-boundary classes.

In equation (11), the parameters most poorly known are in the product cz, which we call the "coupled thickness of seismogenic lithosphere." Therefore, we compute this product by constraining all other variables. The geometric and kinematic parameters of the plate tectonic model (L,v_p,v_o) are available from Bird (2003) (in file PB2002_steps.dat). The line integral of the right side of (11) is restricted to nonorogen regions and subdivided into seven subintegrals for each of the plate-boundary classes. We require equations (11, 12) to hold for each boundary class separately.

To compute the coupled thickness it is only necessary to assume mean values for μ and θ in each plate-boundary class. In continental plate boundaries (CRB, CTF, CCB) virtually all earthquakes are produced in the upper crust, so we estimate elastic shear modulus as $27.7^{+6.3}_{-5.6}$ GPa, corresponding to a P-wave velocity of 5600^{+600}_{-600} m/sec, density of 2650 kg/m^3, and Poisson's ratio of 0.25. In OSR and OTF boundaries, earthquakes are also produced (primarily) in the crust, but because of its more mafic composition we estimate μ as $25.7^{+5.2}_{-4.7}$ GPa, corresponding to a P-wave velocity of 5200^{+500}_{-500} m/sec and density of 2850 kg/m^3. In SUB and OCB

Table 5
Moment Rates, Coupled Lithosphere Thicknesses, and Coupling by Plate-Boundary Class

	Class									
	CRB	CTF	CCB	OSR		OTF			OCB	SUB
	Continental Rift Boundary	Continental Transform Fault	Continental Convergent Boundary	Normal Faulting	Other Mechanism	Slow, 3–39 mm/a	Medium, 40–68 mm/a	Fast, ≥69 mm/a	Oceanic Convergent Boundary	SUB-duction Zone
CMT moment rate*, N m/sec	8.63×10^{11}	3.45×10^{12}	2.75×10^{12}	2.01×10^{11}	1.54×10^{11}	3.14×10^{12}	7.91×10^{11}	7.26×10^{11}	3.17×10^{12}	5.17×10^{13}
Events, 1977–2002.9*	285.9	198.5	259.4	424.3	77	398	406.9	376.6	117.7	2052.8
over threshold, M_t,Nm	1.13×10^{17}	3.5×10^{17}	3.5×10^{17}	1.13×10^{17}	1.13×10^{17}	2×10^{17}	2×10^{17}	2×10^{17}	3.5×10^{17}	3.5×10^{17}
Slope, β	0.65 ± 0.11	0.65 ± 0.12	0.62 ± 0.10	$0.92^{+.07}_{-.32}$	$0.82^{+0.17}_{-0.33}$	0.64 ± 0.08	0.65 ± 0.11	0.73 ± 0.11	0.53 ± 0.13	0.64 ± 0.04
Twentieth century corner magnitude, m_c	$7.64^{+0.77}_{-0.26}$	$8.01^{+0.47}_{-0.21}$	$8.46^{+?}_{-0.39}$	$5.86^{+0.19}_{-0.16}$	$7.39^{+?}_{-0.70}$	$8.14^{+?}_{-0.42}$	$6.55^{+0.27}_{-0.16}$	$6.63^{-0.38}_{-0.17}$	$8.04^{+0.52}_{-0.22}$	$9.58^{+?}_{-0.46}$
Model moment rate§,	$1.67^{+2.62}_{-0.44}$	$3.8^{+3.0}_{-0.9}$	$1.06^{+?}_{-0.43}$	$6.7^{+3.0}_{-3.5}$	$1.9^{+?}_{-0.7}$	$6.7^{+?}_{-2.8}$	$9.4^{+3.4}_{-0.6}$	$9.0^{+3.6}_{-1.2}$	$4.6^{+5.9}_{-1.4}$	$2.85^{+?}_{-1.24}$
N m/s	$\times10^{12}$	$\times10^{12}$	$\times10^{13}$	$\times10^{11}$	$\times10^{11}$	$\times10^{12}$	$\times10^{11}$	$\times10^{11}$	$\times10^{12}$	$\times10^{14}$
Length,* km	18,126	19,375	12,516	61,807	61,807	27,220	10,351	6,331	13,236	38,990
Mean* velocity, mm/a	18.95	21.54	18.16	46.40	7.58	20.68	57.53	97.11	19.22	61.48
Assumed dip θ, deg	$55\pm10°$	$73\pm7°$	$20\pm5°$	$55\pm10°$	$55\pm10°$	$73\pm7°$	$73\pm7°$	$73\pm7°$	$20\pm5°$	14°
Assumed μ, GPa	$27.7^{+6.3}_{-5.6}$	$27.7^{+6.3}_{-5.6}$	$27.7^{+6.3}_{-5.6}$	$25.7^{+5.2}_{-4.7}$	$25.7^{+5.2}_{-4.7}$	$25.7^{+5.2}_{-4.7}$	$25.7^{+5.2}_{-4.7}$	$25.7^{+5.2}_{-4.7}$	49^{+21}_{-21}	49^{+21}_{-21}
μ cosec $\theta\int\sqrt{v_p^2+v_o^2\sec^2\theta}\,dl$, N/sec	$5.5^{+2.4}_{-1.2}\times10^8$	$4.4^{+1.9}_{-1.0}\times10^8$	$6.0^{+3.6}_{-2.0}\times10^8$	$5.0^{+2.3}_{-1.2}\times10^9$	$4.7^{+1.8}_{-1.3}\times10^8$	$5.2^{+1.7}_{-0.9}\times10^8$	$5.3^{+1.3}_{-0.9}\times10^8$	$5.5^{+1.6}_{-0.9}\times10^8$	$1.2^{+1.0}_{-0.9}\times10^9$	$1.58^{+0.67}_{-0.67}\times10^{10}$
Coupled thickness $c\,z$, km	$3.0^{+7.0}_{-1.4}$	8.6^{+11}_{-4}	$18^{+?}_{-11}$	$0.13^{+0.13}_{-0.09}$	$0.40^{+?}_{-0.21}$	$13^{+?}_{-7.3}$	$1.8^{+1.1}_{-0.5}$	$1.6^{+1.1}_{-0.5}$	$3.8^{+13.7}_{-2.3}$	$18.0^{+?}_{-10.8}$
Assumed seis. lith. z, km	6	12	13	8	8	14	14	14	14(?)	26§
$0\le$ Coupling $c\le1$	$0.50^{+0.50}_{-0.23}$	$0.72^{+0.28}_{-0.34}$	$1.00^{+0}_{-0.49}$	$0.016^{+0.016}_{-0.011}$	$0.05^{+0.95}_{-0.03}$	$0.93^{+0.07}_{-0.03}$	$0.13^{+0.08}_{-0.03}$	$0.11^{+0.08}_{-0.03}$	$0.27^{+0.73}_{-0.16}$	$0.69^{+0.31}_{-0.41}$
Limit on m_c (as $c\le1$)	(<8.53)	(<8.60)	<8.61		<12.71	<8.46			(<9.22)	<10.16
Limit on m_c (as $c\le1$, if, $\beta=0.63$)	<8.40	(<8.49)	<8.67		<9.5	<8.41			(<9.99)	<10.06

*Excluding earthquakes and plate-boundary steps inside the 13 orogens.
§From 14 to 40 km below sea level (Oleskevich *et al.*, 1999).
All ranges are 95% confidence limits.

boundaries, the cycle of strain accumulation and release involves both crust and mantle rocks, and it is not clear how their moduli should be averaged. Therefore, we use a rather uncertain mean $\mu = 49^{+21}_{-21}$ GPa to encompass both crustal and mantle values.

Our assumed values of mean fault dip for simple extensional and compressional plate boundaries (CRB, OSR, OSR, OCB) are based on an expectation that a new dip-slip fault in a homogeneous layer of friction 0.85 will form with a dip of 65° or 25°, respectively. However, finite strain and strain-weakening result in rotation of dip-slip faults to smaller dips, for examples, 45° and 15°, respectively. So we estimate mean $\theta = 55 \pm 10°$ for CRB and OSR and $20 \pm 5°$ for CCB and OCB. The dip of subduction zones typically increases from ~8° at the trench to ~30° at the volcanic arc, but not all of this interplate boundary is seismic. In a survey of 12 profiles of four subduction zones, Oleskevich *et al.* (1999) found a mean width of 104 km (and range, 52–201 km) for the seismogenic zone, a mean initial depth ~14 km, and mean maximum depth ~40 km below sea level. Therefore, the mean dip of the seismogenic portions of these zones is $\arctan((40 - 14)/104) = 14°$.

Transform boundaries CTF and OTF are problematic because (11) does not permit $\theta = 90°$ to be assumed in the (general) case of $v_o \neq 0$. There are two obvious possibilities: (1) v_o causes pure dip-slip events on secondary faults that dip gently and share the strike of the primary vertical plate boundary; (2) nonideal transform faults have a steep but nonvertical dip that accommodates both velocity components with a single oblique slip vector. Although we cannot reliably select the active fault plane from most moment tensors, we can examine the distribution of plunges of their *N* (intermediate) principal axes. Under hypothesis 1 we would expect a primary peak at 90° and a secondary peak at 0°; under hypothesis 2 we would expect a single broad peak between 45° and 90°. A histogram of *N*-axis plunges for the 1991 OTF events (outside orogens) has its highest peak at 90°, a secondary peak at 73°, and a minimum at 0°. We somewhat discount the isolated peak at 90° as a possible artifact (of the initialization of the iterative CMT algorithm) because it has no support at adjacent near-vertical angles. A histogram of *N*-axis plunges for the 513 CTF events (outside orogens) shows a much less regular distribution with primary peak at 76°, secondary peak at 13°, and no peaks at 90° or 0°. Of the two end-member hypotheses, the second seems the better approximation. We have computed model moment rates of OTF and CTF boundaries using mean $\theta = 73 \pm 7°$.

The results (Table 5) are coupled thickness (cz) values ranging from a low of 0.13 km (OSR/normal faulting) to highs of 18 km (CCB and SUB). The ranges shown are 95% confidence intervals, taking into account both the uncertainty in the seismic moment rate and the uncertainty in the tectonic model. These coupled thickness values provide a simple description of the seismic moment production of different types of plate boundary that can be used (together with β and m_c) to compute Poissonian models of their predicted seismicities and seismic hazards. In such models it would be best to assume the same values of mean μ and mean θ that were assumed here, unless local evidence contradicts our estimates.

Quantifying certain aspects of seismic hazard may also require "worst-case" upper limits on corner magnitudes. Tables 3 and 4 show that we have only been able to determine this by maximum-likelihood analysis of subcatalogs in certain cases (CRB, CTF, OSR/normal faulting, OTF/medium velocity and high velocity, OCB). No empirical upper limit on the corner magnitude was found for the dangerous CCB and SUB boundaries, which often lie near populated areas. To remedy this, we follow the procedure of Kagan (2002b) and others. Because coupling cannot exceed unity, we estimate a value for the seismogenic lithosphere thickness z, use the tectonic model to find the upper limit on moment rate (considering uncertainties in θ and μ), and finally adjust the corner magnitude until the integral of the tapered Gutenberg-Richter distribution (12) equals this limiting moment rate. These alternative upper limits on corner magnitude are shown in the bottom two rows of Table 5. One is computed using the current best estimate of β, and the other with the "universal" value $\beta = 0.63$ (Kagan, 1999), which is consistent with all of our results on the estimation of β.

Another result of independently estimating z is that bounds can be placed on the seismic coupling coefficient c. These assumed values of z will not be assigned their own error bounds, because in this last step of the analysis it is simple for the reader to substitute any preferred value. Seismogenic lithosphere thickness for CCB boundaries is estimated as 13 km, based on a typical base of the seismogenic layer at 15 km depth (Jackson *et al.,* 1995) and a common aseismic interval in the upper 0–5 km, where blind thrusts produce anticlines (Berberian, 1995). Seismogenic lithosphere thickness of CTF boundaries is estimated as 12 km, based primarily on the well-studied case of California (figure 4 of Bird and Kong, 1994). (Although some CTF boundaries like the Dead Sea rift have lower heat flow and a thicker seismogenic layer, much of the total length of CTF boundaries lies offshore in backarc rifts where the heat flow is higher than the average in California.) Seismogenic lithosphere thickness of OSR boundaries is known only from very limited OBS surveys or from centroid depths of individual large earthquakes; it appears to be approximately 8 km (e.g., 2.4–6.2 km, Huang *et al.,* [1986]; 2–8 km, Huang and Solomon [1987]; 4–12 km, Solomon *et al.* [1988]; ~8 km, Bird *et al.* [2002] interpretation of Watanabe *et al.* [1992]; ~8 km, Tilmann *et al.* [2003]). We are not aware of relevant studies on CRB boundaries, so we rather arbitrarily assign them a seismogenic lithosphere that is slightly thinner (6 km) based on the lower creep-activation temperatures in continental crust. OTF boundaries have (on average) lower heat flow and thicker seismogenic lithosphere of ~14 km (5.2–11.7 km [to 400°C], Engeln *et al.* [1986]; 7–10 km [centroid depths] or 14–20 km [twice centroid depths], Bergman and

Solomon [1988]; 6.4–13.3 km [thermal model], Okal and Langenhorst [2000]). OCB boundaries have not been studied, so we arbitrarily assign them the same thickness. The seismogenic thickness of SUB boundaries is taken as 26 km (from 14 to 40 km below sea level), so that with our assumed mean dip of 14°, the mean width of the seismogenic zone will be 104 km, as observed (Oleskevich *et al.,* 1999; discussed previously). (We note an alternative estimate of $z = 52 - 15 = 37$ km, based on the central 90% of the moment release distribution by Zhang and Schwartz (1992). However, their study considered only earthquakes of $5 < m < 7$, which release only about 3%–16% of total moment and made no correction for the inflation of apparent z by earthquake mislocations.)

The inferred coupling coefficients then range (using best estimates) from a low of 0.016 for normal faulting on OSRs to a high of 1.0 in CCBs. The coupling values that are computed to be less than unity with 95% confidence are OSR/normal faulting, $0.016^{+0.016}_{-0.011}$; OTF/medium velocity, $0.12^{+0.09}_{-0.04}$; and OTF/high velocity, $0.11^{+0.08}_{-0.05}$. Comparing results with our previous study (Bird *et al.,* 2002), we confirm the low coupling of most OSRs and OTFs, except that we now add two qualifications: (1) Strike-slip events on OSRs probably have low coupling (best estimate, 0.05), but perfect coupling cannot be formally excluded because of the lack of an upper limit on the corner magnitude. (However, by assuming that the corner magnitude is not more than 9, we compute a soft upper bound of 0.19 for coupling.) (2) Slow-moving OTF boundaries (<40 mm/a) may have high, or even perfect, coupling.

Discussion

Our hope when planning this project was that using all the large shallow earthquakes recorded during 103 years would yield enough events to bound corner magnitudes with a firm upper limit using earthquake statistics alone. That would enable us to place upper limits on coupled lithosphere thickness. In some settings we succeeded (CRB, CTF, OSR/normal faulting, medium and fast OTF, OCB) and in other settings we failed (CCB, OSR/strike slip, slow OTF, SUB). In the latter cases we were able to use the constraint that coupling is no more than unity to find alternate (model-dependent) upper limits on corner magnitude. The large residual uncertainties that we encountered in all cases show that it is probably impossible to accurately measure coupled thickness or coupling with smaller data sets, such as those restricted to a single subduction zone (McCaffrey, 1997). This could only be done by making use of paleoseismic records that were far more extensive, accurate, and complete than any yet published.

Another issue we did not resolve is to what extent coupling in certain plate boundaries may be velocity dependent. Investigating this question requires subdividing subcatalogs further, reducing event counts, and increasing uncertainties. Except in the OSR boundaries (where velocity dependence was shown by Bird *et al.*, 2002) and OTF boundaries (where we find that slow boundaries are more strongly coupled), we have not searched for possible velocity dependence. If there is any, our coupling figures must be considered as averages.

The passage of time will reduce the uncertainties in future studies by expanding the catalog of large earthquakes, but this will take centuries. In the short term, the plate-model part of the calculation might be improved by more tightly constraining elastic moduli and fault dips. The largest twentieth-century earthquakes in each subcatalog should probably be studied individually to verify their moments and locations and correct any misclassifications; this work has begun (e.g., Kanamori and Cipar, 1974) but is not finished. Meanwhile, expansion of seismic networks will lower the completeness threshold of catalogs, allowing β to be better determined. Better knowledge of β will then allow the large historic earthquakes already in the catalog to better constrain the corner magnitude by quantifying the curvature of log-frequency/magnitude plots.

In our study, we found some interesting variations in maximum-likelihood estimates of β, from a low of 0.53 for OCB to a high of 0.92 for OSR/normal faulting. However, we did not find any cases where apparent differences in β could be stated with 95% confidence. In fact, all the 95% confidence limits we found overlap in a common range of $0.61 \leq \beta \leq 0.66$. As Kagan (1999) proposed, the "null hypothesis" should be that β is everywhere uniform and that apparent variations are due to small catalogs, mixed earthquake populations, or inappropriate statistics. This null hypothesis has not yet been rejected for any tectonic setting of global scope.

In contrast, we find that at least four distinct values of corner magnitude seem to be required. Based on the 95% confidence limits in Table 5, these are OSR normal faulting (range, 5.70–6.05); OTF medium and fast velocities (range, 6.39–7.01); CRB/CTF/CCB/OTF slow velocity/OCB (range, 7.38–8.67); and SUB (range, 9.12–?).

Another premise of our study is that it would be valuable to divide shallow earthquakes into seven tectonic settings. (This was motivated by the clearly different corner magnitudes of OSR and SUB.) Retrospectively, we see that most of these distinctions resulted in interesting variations in seismicity rate (Table 2) and/or frequency/magnitude parameters (Tables 3 and 4) and/or coupling (Table 5). An exception is the distinction between medium-velocity and high-velocity OTFs, which turned out to be unnecessary. Another possible amalgamation would be to group CTFs with slow OTFs, because they have similar corner magnitudes and coupling at similar mean plate velocities of ~21 mm/a. On the other hand, the relatively high corner magnitude of slow OTFs rests on only six $m > 7.2$ earthquakes in 103 years, versus 30 on CTFs. (The total length of slow OTFs outside orogens is 9% greater than the total length of CTFs outside orogens.) If the earthquake populations were truly identical, the probability of obtaining two samples as different as 6 and 30 would be very small ($\sim 10^{-5}$). We should also con-

sider the alternative that the present slow-OTF subcatalog may be an accidental composite, with one component of low coupling and corner magnitude ~7.1 (as inferred by Bird *et al.*, 2002) and another component of low β and high m_c (similar to OCBs).

In general, the slow-OTF subcatalog is not the only oceanic subcatalog that seems to show "outlier" events fitting poorly with the rest of the distribution (at least, under the assumption of a tapered Gutenberg-Richter distribution). This is also seen in the OSR and OCB distributions based on CMT and in the SUB distribution based on the merged catalog. (Ⓔ Refer to graphs in the electronic supplement that is available online at the SSA Web site.) Some may interpret this as evidence for some "characteristic earthquakes" of large size that are more frequent than they are assumed to be in the tapered Gutenberg-Richter distribution. However, in the case of OSR we found that these large "outlier" events could be eliminated by restricting the subcatalog to only events of normal-faulting mechanism. We suspect that other seafloor plate boundaries have unmodeled geometric complexities as well, with the result that small numbers of inappropriate mechanisms are mixed into some of our distributions. It remains unclear whether we have enough data for any tectonic setting to prove the existence of characteristic earthquakes.

With the possible exception of slow OTF boundaries, most of our results show a consistent and significant difference in coupling between the continental settings (CRB, CTF, CCB) and oceanic settings (OSR, OTF, OCB). Subduction zones, which have intermediate or mixed crustal character, appear more similar to the continental group. This distinction should definitely be taken into account in thinking about seismic gaps, by which we mean plate-boundary segments that had no large earthquakes in the twentieth century.

The mean of the three best-estimate coupling figures in the continents is 74%, which indicates generally good coupling with some local exceptions. Such behavior is familiar to us in California, where certain segments of the San Andreas and Hayward-Calaveras faults are creeping whereas the majority of regional faults are seismic. (However, the figures in Table 5 are independent of California data, because in model PB2002 California is in an orogen.) In continental settings, it should be assumed that all seismic gaps are dangerous unless there is direct geodetic evidence of creep at rates comparable with relative plate velocities. For example, the Himalayan frontal fault system can and will produce future great earthquakes (Triep and Sykes, 1997; Cattin and Avouac, 2000; Rong, 2002; Rong and Jackson, 2002) despite its relative quiescence during the epoch of the CMT catalog.

However, by proposing continental seismic gaps as possible places of large future earthquakes, we do not mean that the rate or the probability of these future events is necessarily larger than in similar boundary segments that have been active recently (Rong *et al.,* 2003), as suggested by the traditional interpretation of seismic gaps (Nishenko, 1991). Although some "gap" segments accumulate tectonic deformation that should be released by earthquakes, the seismic potential of these boundary intervals in the near future is presently unknown.

In this continental environment where the majority of seismic gaps are locked (and therefore temporary), projection of seismic hazard by extrapolation of CMT seismicity (e.g., Jackson and Kagan, 1999; Kagan and Jackson, 2000) will only work well during relatively short time windows in which there are aftershocks and other triggered earthquakes. For successful longer-term projections, it will be necessary to build in a kinematic model of tectonics.

In deep-sea settings (OSR, OCB, and most OTFs, omitting the slow subcategory), the mean of the best-estimate coupling figures is 12%, which indicates that aseismic creep is the dominant mode and that seismic fault patches are exceptional. We do not yet know whether these seismic fault patches are fixed in space by special local conditions, or whether they arise spontaneously in unpredictable locations from some kind of nonlinear dynamics of unsteady fault creep. Additional centuries of earthquake recording will settle the question. (An answer may be available sooner if seafloor geodesy becomes practical, because then we can monitor fault creep directly and watch for variations.) If it turns out that seismic fault patches in the seafloor are fixed in space, because they are defined by special fault geometries (e.g., tectonic knots) or special geology, then seismic hazard prediction by extrapolation of CMT seismicity (e.g., Jackson and Kagan, 1999; Kagan and Jackson, 2000) should enjoy both short-term and long-term success in these settings.

Acknowledgments

Research supported by the U.S. Geological Survey (USGS), Department of the Interior, under USDOI award no. 01HQGR0021. The views and conclusions contained in this document are those of the authors and should not be interpreted as necessarily representing the official policies, either expressed or implied, of the U.S. Government. Research was also partly supported by the Southern California Earthquake Center (SCEC). SCEC is funded by National Science Foundation Cooperative Agreement EAR-0106924 and USGS Cooperative Agreement 02HQAG0008. Publication 749, SCEC.

References

Berberian, M. (1995). Master "blind" thrust faults hidden under the Zagros folds: active basement tectonics and surface morphotectonics, *Tectonophysics* **241,** 193–224.

Bergman, E., and S. Solomon (1988). Transform-fault earthquakes in the North Atlantic: source mechanisms and depth of faulting, *J. Geophys. Res.* **93,** 9027–9057.

Bird, P. (2003). An updated digital model of plate boundaries, *Geochem. Geophys. Geosystems* **4,** 1027, doi 10.1029/2001GC000252.

Bird, P., and X. Kong (1994). Computer simulations of California tectonics confirm very low strength of major faults, *Geol. Soc. Am. Bull.* **106,** 159–174.

Bird, P., Y. Y. Kagan, H. Houston, and D. D. Jackson (2000). Earthquake potential estimated from tectonic motion (abstract), *Eos Trans. AGU* **81,** no. 48 (Fall Meeting Supplement), F1226–F1227.

Bird, P., Y. Y. Kagan, and D. D. Jackson (2002). Plate tectonics and earthquake potential of spreading ridges and oceanic transform faults, in *Plate Boundary Zones, Geodynamics Series* **30,** S. Stein and J. T. Freymueller (Editors), American Geophysical Union, Washington, D.C., 203–218.

Cattin, R., and J. P. Avouac (2000). Modeling mountain building and the seismic cycle in the Himalaya of Nepal, *J. Geophys. Res.* **105,** 13,389–13,407.

Cifuentes, I. L., and P. G. Silver (1989). Low-frequency source characteristics of the great 1960 Chilean earthquake, *J. Geophys. Res.* **94,** 643–663.

DeMets, C., R. G. Gordon, D. F. Argus, and S. Stein (1990). Current plate motions, *Geophys. J. Int.* **101,** 425–478.

Dziewonski, A. M., T.-A. Chou, and J. H. Woodhouse (1981). Determination of earthquake source parameters from waveform data for studies of global and regional seismicity, *J. Geophys. Res.* **86,** 2825–2852.

Ekström, G., and M. Nettles (1997). Calibration of the HGLP seismograph network and centroid-moment tensor analysis of significant earthquakes of 1976, *Phys. Earth Planet. Int.* **101,** 221–246.

Ekström, G., A. M. Dziewonski, N. N. Maternovskaya, and M. Nettles (2003). Global seismicity of 2001: centroid moment tensor solutions for 961 earthquakes, *Phys. Earth Planet. Int.* **136,** no. 3–4, 165–185.

Engdahl, E. R., and A. Villaseñor (2002). Global seismicity: 1900–1999, in *IASPEI Handbook of Earthquake and Engineering Seismology*, W. H. K. Lee, P. Jennings, H. Kanamori, and C. Kisslinger (Editors), Academic Press, Boston, 665–690.

Engeln, J. F., D. A. Wiens, and S. Stein (1986). Mechanisms and depths of Atlantic transform earthquakes, *J. Geophys. Res.* **91,** 548–477(?).

Hanks, T. C., and H. Kanamori (1979). A moment magnitude scale, *J. Geophys. Res.* **84,** 2348–2350.

Holt, W. E., N. Chamot-Rooke, X. Le Pichon, A. J. Haines, B. Shen-Tu, and J. Ren (2000). Velocity field in Asia inferred from Quaternary fault slip rates and Global Positioning System observations, *J. Geophys. Res.* **105,** 19,185–19,209.

Huang, P. Y., and S. C. Solomon (1987). Centroid depths and mechanisms of mid-ocean ridge earthquakes in the Indian Ocean, Gulf of Aden, and Red Sea, *J. Geophys. Res.* **92,** 1361–1382.

Huang, P. Y., S. C. Solomon, E. A. Bergman, and J. L. Nabalek (1986). Focal depths and mechanisms of Mid-Atlantic Ridge earthquakes from body wave inversion, *J. Geophys. Res.* **91** no. B1, 579–598.

Jackson, D. D., and Y. Y. Kagan (1999). Testable earthquake forecasts for 1999, *Seism. Res. Lett.* **70,** 393–403.

Jackson, J., J. Haines, and W. Holt (1995). The accommodation of Arabia-Eurasia plate convergence in Iran, *J. Geophys. Res.* **100,** 15,205–15,220.

Kagan, Y. Y. (1991a). Seismic moment distribution, *Geophys. J. Int.* **106,** 123–134.

Kagan, Y. Y. (1991b). 3-D rotation of double-couple earthquake sources, *Geophys. J. Int.* **106,** 709–716.

Kagan, Y. Y. (1999). Universality of the seismic moment-frequency relation, *Pure Appl. Geophys.* **155,** 537–573.

Kagan, Y. Y. (2002a). Seismic moment distribution revisited. I. Statistical results, *Geophys. J. Int.* **148,** 520–541.

Kagan, Y. Y. (2002b). Seismic moment distribution revisited. II. Moment conservation principle, *Geophys. J. Int.* **149,** 731–754.

Kagan, Y. Y. (2003). Accuracy of modern global earthquake catalogs, *Phys. Earth Planet. Int.* **135,** no. 2-3, 173–209, doi 10.1016/S0031-9201(02)00214-5.

Kagan, Y. Y., and D. D. Jackson (2000). Probabilistic forecasting of earthquakes, *Geophys. J. Int.* **143,** 438–453.

Kanamori, H., and J. J. Cipar (1974). Focal process of the great Chilean earthquake May 22, 1960, *Phys. Earth Planet. Int.* **9,** 128–136.

Kreemer, C., W. E. Holt, and J. Haines (2002) The global moment rate distribution within plate boundary zones, in *Plate Boundary Zones, Geodynamics Series* **30,** S. Stein and J. T. Freymueller (Editors), American Geophysical Union, Washington, D.C., 173–190.

McCaffrey, R. (1997). Statistical significance of the seismic coupling coefficient, *Bull. Seism. Soc. Am.* **87,** 1069–1073.

Massell, C., M. F. Coffin, P. Mann, S. Mosher, C. Frohlich, C. S. Duncan, G. Karner, D. Ramsay, and J.-F. Lebrun (2000). Neotectonics of the Macquarie Ridge Complex, Australia-Pacific plate boundary, *J. Geophys. Res.* **105,** 13,457–13,480.

Nishenko, S. P. (1991). Circum-Pacific seismic potential: 1989–1999, *Pure Appl. Geophys.* **135,** 169–259.

Okal, E. A., and A. R. Langenhorst (2000). Seismic properties of the Eltanin Transform system, South Pacific, *Phys. Earth Planet. Int.* **119,** 185–208.

Oleskevitch, D. A., R. D. Hyndman, and K. Wang (1999). The updip and downdip limits to great subduction earthquakes: Thermal and structural models of Cascadia, south Alaska, SW Japan, and Chile, *J. Geophys. Res.* **104,** 14965–14991.

Pacheco, J. F., and L. R. Sykes (1992). Seismic moment catalog of large, shallow earthquakes, 1900–1989, *Bull. Seism. Soc. Am.* **82,** 1306–1349.

Pacheco, J. F., L. R. Sykes, and C. H. Scholz (1993). Nature of seismic coupling along simple plate boundaries of the subduction type, *J. Geophys. Res.* **98,** 14133–14159.

Rong, Y.-F. (2002). Evaluation of earthquake potential in China, *Ph.D. Thesis*, University of California, Los Angeles.

Rong, Y.-F., and D. D. Jackson (2002). Earthquake potential in and around China: estimated from past earthquakes, *Geophys. Res. Lett.* **29,** no. 16, 1780, doi 10.1029/2002GL015297.

Rong, Y.-F., D. D. Jackson, and Y. Y. Kagan (2003). Seismic gaps and earthquakes, *J. Geophys. Res.*, **108,** no. B10, 2471, ESE-6, doi 10.1029/2002JB002334.

Ruff, L., and H. Kanamori (1980). Seismicity and the subduction process, *Phys. Earth Planet. Int.* **23,** 240–252.

Solomon, S. C., P. Y. Huang, and L. Meinke (1988). The seismic moment budget of slowly spreading ridges, *Nature* **334,** 58–60.

Tilmann, R., L. Planert, T. Reston, E. Flueh, and W. Weinrebe (2003). Micro-earthquake seismicity of the Mid-Atlantic Ridge at 5°S: A different style of tectonic extension, *Eos Trans. AGU* **84,** no. 46, abstract T12D-0501.

Triep, E. G., and L. R. Sykes (1997). Frequency of occurrence of moderate to great earthquakes in intracontinental regions: Implications for changes in stress, earthquake prediction, and hazards assessment, *J. Geophys. Res.* **102,** no. B5, 9923–9948.

Watanabe, T., S. Kodaira, H. Shiobara, T. Kanazawa, R. Stefansson, G. B. Gudmundsson, and H. Shimamura (1992). Microseismicity in the Reykjanes Ridge, July 1990: hypocenter distribution derived from an OBS array, *Zisin* Ser. 2, **45,** 327–337.

Zhang, Z., and S. Y. Schwartz (1992). Depth distribution of moment release in underthrusting earthquakes at subduction zones, *J. Geophys. Res.* **97,** 537–544.

Department of Earth and Space Sciences
University of California
Los Angeles, California 90095-1567
pbird@ess.ucla.edu
ykagan@ucla.edu

Manuscript received 30 May 2003.